International Journal of Solids and Structures 331 (2026) 113896

Contents lists available at ScienceDirect

International Journal of Solids and Structures

journal homepage: www.elsevier.com/locate/ijsolstr

Ductile-to-brittle transition in high-strength steel: Experiments and damage-coupled constitutive modeling

Zhichao Wei *, Guoxi Mao, Dongsong Li, Berk Tekkaya, Sophie Stebner, Sebastian Münstermann

Institute of Metal Forming, RWTH Aachen University, Intzestr. 10, D-52072 Aachen, Germany

ARTICLE INFO

Keywords:
Sub-size Charpy experiments
Ductile-to-brittle
Ductile damage and fracture
Cleavage fracture
Numerical simulations

ABSTRACT

This paper focuses on the experimental and numerical analysis of the ductile-to-brittle behavior of the high-strength low-alloy (HSLA) steel. Different uniaxial experiments, using samples manufactured from 2 mm thick sheet metal and covering a wide range of stress states, were conducted to identify the elastic, plastic, and ductile damage and fracture loci, and the details of the experimental–numerical hybrid identification strategy are discussed. In addition, a series of sub-sized V-notch Charpy tests from room temperature to -196°C were performed to investigate the ductile-to-brittle transition behavior. For numerical simulations, a modified Bai and Wierzbicki stress-state-dependent yield condition considering isotropic damage by incorporating a scalar damage variable is used to capture the elastic–plastic-damage behavior. The damage evolution is driven by energy dissipation. An extended stress-triaxiality-dependent Johnson–Cook-type damage and fracture model is developed by incorporating the Lode angle parameter to capture the initiation of ductile damage and fracture more accurately. Moreover, a novel temperature-dependent stress-based criterion is introduced to model brittle fracture. The proposed damage and fracture continuum framework accurately captures and predicts the ductile-to-brittle material behavior and can serve as an alternative to the traditional fracture toughness method for characterizing fracture behavior.

1. Introduction

With technological progress and the growing demand for efficient resource utilization, increasing requirements are being placed on materials and structures in lightweight construction. In this context, special attention must be paid to accurate descriptions of the inelastic behavior of materials in numerical modeling of deformation and damage in lightweight structures. The High-strength low-alloy (HSLA) steel is renowned for its versatility and is increasingly used in industries such as bridge construction, crane manufacturing, mechanical engineering, and offshore platforms. Thus, it is essential to understand material behavior under different loading conditions to ensure safe and effective use of materials.

Numerical prediction of ductile damage and fracture is essential for characterizing mechanical behavior, as damage degrades material properties. Ductile damage is mainly caused by the localization of plastic deformations. Thus, accurately predicting plastic deformations is also important for capturing the initiation and evolution of damage, as well as the onset of fracture. Spitzig and Richmond (1984) observed the influence of hydrostatic stress on the onset of plastic yielding in metals, known as the stress-differential (SD) effect, which has also been reported in the literature (Brünig, 1999; Bai and Wierzbicki, 2008; Voyiadjis et al., 2013; Wei et al., 2022, 2025a; Pan et al., 2025). Among these studies, Spitzig and Richmond (1984) pointed out that hydrostatic stress has a negligible influence on the evolution of plastic strain. In contrast, other researchers reported that neglecting the influence of hydrostatic pressure on hardening behavior can lead to inaccurate numerical predictions compared with experimental results, as discussed in Bai and Wierzbicki (2008) and Voyiadjis et al. (2013).

Furthermore, ductile damage and fracture are known to be stress-state-dependent (Lian et al., 2013, 2015; Mohr and Marcadet, 2015; Lou et al., 2017; Habibi et al., 2024; Wei et al., 2025d,b, 2024a). Ductile damage occurs due to the nucleation, growth, and coalescence of micro-voids, eventually leading to crack formation. It is also observed in uniaxial tension (Dogbone and round bar) specimens that fracture initiates at the center of the geometry and propagates outward, forming a typical cup-cone fracture surface. Concerning the numerical modeling of ductile damage, two main approaches are widely used: micromechanically motivated models (Gurson, 1977; Tvergaard and Needleman, 1984; Xue, 2008; Nahshon and Hutchinson, 2008; Wu

* Corresponding author.
E-mail address: zhichao.wei@ibf.rwth-aachen.de (Z. Wei).

https://doi.org/10.1016/j.ijsolstr.2026.113896
Received 1 December 2025; Received in revised form 18 January 2026; Accepted 8 February 2026
Available online 10 February 2026
0020-7683/© 2026 The Authors. Published by Elsevier Ltd. This is an open access article under the CC BY-NC-ND license (http://creativecommons.org/licenses/by-nc-nd/4.0/).

et al., 2022), which incorporate porosity (void fraction) into the plastic model as a softening term, and continuum damage mechanics (CDM) models (Lemaitre and Dufailly, 1987; Brünig, 2003; Lian et al., 2013; Voyiadjis et al., 2013; Wei et al., 2024c; Zistl et al., 2024; Zhang et al., 2025; Pan et al., 2025; Wei et al., 2026). Compared to micromechanically motivated damage models, CDM models offer advantages for characterizing the degradation of elastic properties and are easier to apply in material characterization. In addition, advanced plastic-damage continuum models consider the influence of the stress state in capturing the occurrence and evolution of damage behavior, as shown in Lian et al. (2013) and Wei et al. (2024c, 2026).

Based on numerical and experimental observations, a large number of ductile fracture models, including strain-based (Rice and Tracey, 1969; Johnson and Cook, 1985; Bao and Wierzbicki, 2004; Bai and Wierzbicki, 2008, 2010; Lou and Huh, 2013; Wu et al., 2023; Zeng et al., 2024) and stress-based (Stoughton and Yoon, 2011; Khan and Liu, 2012; Wu and Lou, 2025; Mohr and Marcadet, 2015; Lou and Yoon, 2018; Lou et al., 2022) criteria, have been extensively discussed in the literature. Among them, the Rice and Tracey (1969) and Johnson and Cook (1985) models are two of the most widely used failure models in engineering applications because of their simplicity. However, they are only suitable for high stress triaxiality and show disadvantages in characterizing fracture behavior under shear loading conditions. Several advanced models have been proposed to address the inaccuracies in shear fracture behavior. Bai and Wierzbicki (2008) introduced the Lode angle parameter into the Johnson–Cook-type ductile failure model. Subsequently, the Mohr–Coulomb criterion was transformed into ductile fracture loci in terms of stress triaxiality, Lode parameter, and strain space to describe ductile fracture behavior (Bai and Wierzbicki, 2010). Similarly, Mohr and Marcadet (2015) characterized fracture behavior using an extended Mohr–Coulomb approach that incorporates the Hosford equivalent stress together with the normal stress acting on the plane of maximum shear. In addition, Lou and Huh (2013) introduced an uncoupled model describing ductile fracture governed by void nucleation, growth, and shear coalescence.

Cleavage fracture is a phenomenon in which micro-cracks propagate either through the grains (transgranular) or along grain boundaries (intergranular); cleavage is controlled by the initiation and propagation of these micro-cracks, ultimately resulting in brittle failure (Wei et al., 2025c). Cleavage fracture is usually modeled using a critical principal stress criterion and statistical probability methods. Ritchie et al. (1973) introduced the critical stress concept, where cleavage fracture occurs if the principal stress exceeds a critical value independent of temperature and strain rate. Another approach combines plastic flow with a Weibull probability distribution method, as proposed by the Beremin group (Beremin et al., 1983). Although these approaches have proven effective in capturing cleavage fracture behavior in several metals, they cannot fully describe the mechanisms governing the nucleation and growth of micro-cracks that lead to the softening associated with brittle fracture. In addition, both experimental and numerical studies (Krajcinovic and Fonseka, 1981; He et al., 2017; Tlatlik et al., 2023; Shen et al., 2024) have consistently demonstrated that stress triaxiality plays a key role in cleavage fracture behavior.

It is worth noting that only limited literature focuses on describing the ductile-to-brittle transition mechanism. Needleman and Tvergaard (2000) proposed that ductile damage is caused by the nucleation, growth, and coalescence of micro-voids based on plastic deformation, whereas cleavage fracture is modeled using a temperature and strain rate independent critical stress (Ritchie model Ritchie et al., 1973). Other researchers have also applied similar concepts, such as the local or non-local GTN model incorporated with either the Ritchie or Beremin model (Pineau, 2008; Hütter et al., 2014; Tanguy et al., 2005). Later, Türtük and Deliktaş (2016) used the same GTN thermoplastic model for ductile damage but modified the approach by incorporating the Leckie–Hayhurst creep rupture criterion (Leckie and Hayhurst, 1977) and Lemaitre's (Lemaitre and Dufailly, 1987) CDM concept to simulate brittle damage behavior. It is evident that multiple damage surfaces and different damage mechanisms are combined, merging the porosity theory of the GTN model with the effective area theory from the Lemaitre-based damage model. This combination introduces divergence in the CDM theory. In addition, the importance of stress states and anisotropic damage behavior is not adequately considered in the proposed model, making the results less reliable.

To address the above-mentioned issues, a novel continuum damage model incorporating the stress states in damage initiation and evolution, as proposed by Lian et al. (2013), is introduced to simulate ductile damage and fracture behavior. In addition, a modified Ritchie model (Ritchie et al., 1973), which considers the influence of temperature, is newly introduced in this work to formulate a continuum damage model framework for characterizing the ductile-to-brittle transition behavior. A series of uniaxial experiments covering a wide range of moderate positive stress triaxialities with different Lode angle parameters was performed to study ductile damage and fracture behavior, as well as to identify the necessary material parameters. Compared with the biaxial loading experiments performed by Wei et al. (2023, 2025a), uniaxial experiments do not require specialized testing devices but have limitations for characterizing negative stress triaxialities and low positive stress states. Therefore, several uniaxially loaded specimens, including uniaxial tension with and without notches, central-hole and central-ellipse specimens, and plane-strain specimens, are selected to achieve different stress triaxialities. Among these, plane strain specimens generate high stress states with near-zero Lode angle parameters. With increasing notch radius in plane strain specimens, both the stress triaxiality and the Lode angle parameter decrease. Moreover, notched specimens generate high stress triaxiality with moderate Lode angle parameters, whereas central-hole and central-ellipse specimens exhibit varying stress states depending on notch geometry.

Furthermore, a large number of sub-sized V-notch Charpy tests were designed and performed at different temperatures to experimentally examine the ductile-to-brittle transition behavior of the HSLA steel (Wei et al., 2025c). It should be noted that due to the received high-strength steel sheets having a thickness of only 4 mm, the standard Charpy specimen geometry with a cross-section of 10 mm × 10 mm could not be applied. Therefore, sub-sized Charpy specimens with a reduced thickness of 4 mm were used in this work to study the material behavior. The thickness of Charpy specimens significantly influences toughness, as plane strain conditions become more pronounced in thicker specimens due to increased transverse strain restraint. This results in a smaller plastic zone and lower toughness. In addition, according to the empirical formulation proposed by Wallin (2020), the measured impact energy obtained from sub-sized Charpy specimens can be converted to standard Charpy test values. This conversion was experimentally confirmed by Wei et al. (2025c) through analyses of the transition temperature based on impact energy and scanning electron microscopy images of fracture surfaces using the same HSLA steel and sub-sized Charpy tests, showing that the empirical approach provides reasonable results within engineering accuracy.

This paper is structured as follows. The investigated material and testing geometries are introduced in Section 2. The constitutive model is briefly summarized in Section 3, and the numerical implementation is discussed in Section 4. The material identification strategy is described in detail in Section 5. The experimental and numerical results for the ductile-to-brittle transition behavior are presented in Section 6. Conclusions are provided in Section 7.

2. Materials and experiments

In this work, water-quenched and tempered high-strength low-alloy steel S1100Q is employed to investigate ductile damage and ductile-to-brittle fracture behavior. The chemical composition is summarized in Table 1.

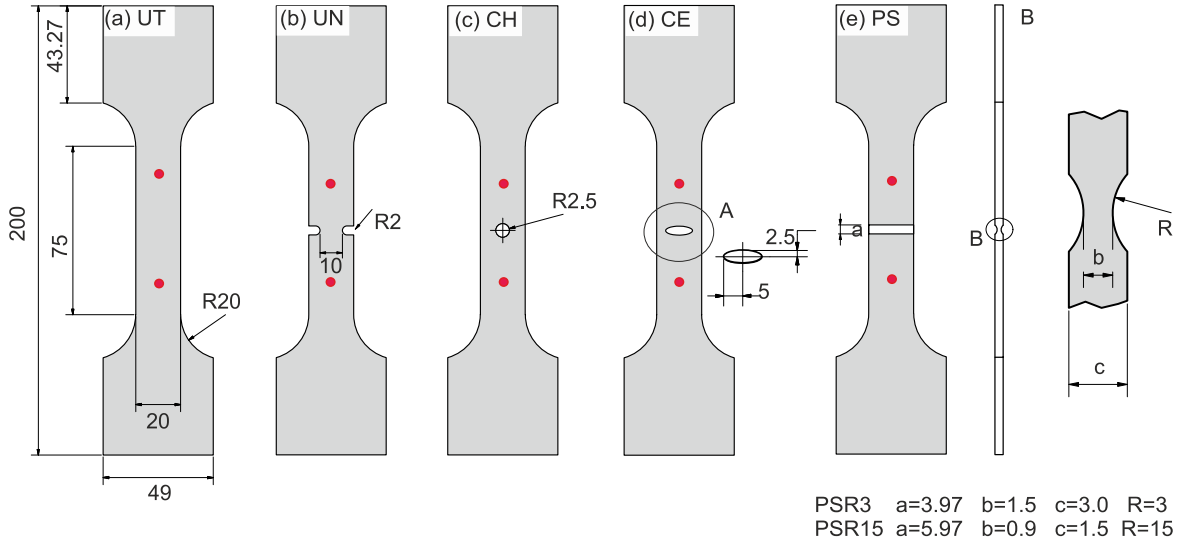


Fig. 1. Sketch of the uniaxially loaded specimens; all units in mm, the thickness for UT, UN, CH, and CE are 2 mm.

Table 1
Chemical composition of high-strength structural steel S1100Q in mass percent.

Fe	Mn	Cr	C	Al
to balance	1.49%	0.31%	0.14%	0.09%
Si	Ti	Cu	Nb	Others
0.05%	0.04%	0.02%	0.02%	0.03%

A series of uniaxial experiments were performed to identify the elastic, plastic, damage, and fracture parameters. The sketches of the specimens are shown in Fig. 1, where the red points indicate the measured points used in the experimental and numerical simulations. The dogbone uniaxial tension (UT) specimen (Fig. 1(a)) is used to calibrate the elastic–plastic parameters, since a homogeneous stress state is generated before necking. In addition, the U-notched (UN) specimen, the central-hole (CH) specimen, the central-ellipse (CE) specimen, and the plane strain specimens with notch radii of 3 mm (PSR3) and 15 mm (PSR15) were tested to obtain a wide range of stress states for calibrating the damage and fracture parameters. It should be mentioned that the displacement is measured using an extensometer during the experiments. The gauge length is 60 mm for the UT specimen (see Fig. 1(a)), whereas it is 40 mm for the other notched specimens, as shown in Fig. 1(b)–(e), where the gauge lengths are marked with red points.

Moreover, sub-size Charpy tests at different temperatures were designed to study the ductile-to-brittle behavior of the investigated material. The geometry is illustrated in Fig. 2. The cross-section is 10 mm × 4 mm, with a V-notch of 45 ° angle, 0.25 mm root radius, and 2 mm depth. It is worth noting that, since the material is a 4 mm metal sheet, the standard Charpy test cannot be applied. However, as this work does not aim to determine the transition point defined by 27 J, the use of sub-sized specimens does not affect the evaluation of the transition behavior. All sub-size Charpy tests were performed using a pendulum impact tester with a hammer mass of 6.90 kg, a maximum capacity of 50 J, and a maximum force of 10 kN. Tests were conducted at 15 temperatures ranging from −196 °C to room temperature (23 °C), using either an alcohol bath or a climatic chamber. Each test was repeated at least twice to ensure reproducibility. Further details of the testing are provided in Wei et al. (2025c).

In addition, the fracture surfaces were characterized using a Zeiss SIGMA scanning electron microscope (SEM) to investigate the associated damage and fracture mechanisms. The observations were performed under high-vacuum conditions with a working distance of 11 mm, a beam diameter of 300 nm, and an accelerating voltage of 20 kV.

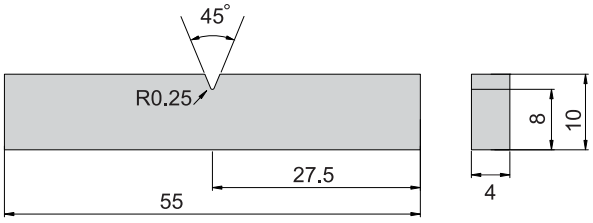


Fig. 2. Sketch of the sub-sized Charpy specimen; all units in mm.

3. Constitutive modeling

In this section, the elastic–plastic-damage model and its implementation, as well as the ductile and fracture criteria, are briefly summarized.

3.1. Stress state variables

The stress triaxiality η and normalized Lode angle parameter $\bar{\theta}$ are used to characterize the stress states. The stress triaxiality is defined as the ratio of the mean stress σ_m and the equivalent stress σ_{eq}, and it is given by

$$\eta = \frac{\sigma_m}{\sigma_{eq}} = \frac{I_1}{3\sqrt{3J_2}} \tag{1}$$

with

$$I_1 = \mathrm{tr}\boldsymbol{\sigma} \quad \text{and} \quad J_2 = \frac{1}{2}\mathrm{dev}\boldsymbol{\sigma} \cdot \mathrm{dev}\boldsymbol{\sigma}\,, \tag{2}$$

where I_1 and J_2 are the stress invariants based on the stress tensor $\boldsymbol{\sigma}$. In addition, the normalized Lode angle parameter is defined as

$$\bar{\theta} = 1 - \frac{6\theta}{\pi} = 1 - \frac{2}{\pi}\arccos\left[\frac{3\sqrt{3}}{2}\frac{J_3}{(J_2)^{3/2}}\right], \tag{3}$$

where $J_3 = \det(\mathrm{dev}\boldsymbol{\sigma})$ is the third stress invariant.

It is clear that the scalar stress triaxiality η and the Lode angle parameter $\bar{\theta}$ can be used to distinguish different loading cases. For example, the stress triaxiality for uniaxial tension and uniaxial compression is $1/3$ and $-1/3$, respectively, with corresponding normalized Lode

angle parameters of 1 and −1. For shear tests, both the stress triaxiality and the Lode angle parameter are equal to 0.

3.2. Plastic-damage modeling

For plasticity, the yielding can be adjusted by changing the Lode angle parameter θ and stress triaxiality η dependency, as indicated by Bai and Wierzbicki (2008). However, the stress triaxiality dependency of metals is usually negligible (Lian et al., 2013), and the yield function incorporating damage-induced softening is given by

$$f^{\mathrm{pl}} = \sigma_{eq} - (1-D) f_p(T)\sigma_y \left[c_\theta^s + (c_\theta^{ax} - c_\theta^s)\left(\beta - \frac{\beta^{m+1}}{m+1}\right)\right] = 0\,, \tag{4}$$

with

$$\beta = \frac{\cos\left(\frac{\pi}{6}\right)}{1-\cos\left(\frac{\pi}{6}\right)}\left(\frac{1}{\cos(\theta-\frac{\pi}{6})}-1\right) \quad \text{and} \quad c_\theta^{\mathrm{ax}} = \begin{cases} c_\theta^{\mathrm{t}} & \bar{\theta} \geq 0 \\ c_\theta^{\mathrm{c}} & \bar{\theta} < 0 \end{cases}, \tag{5}$$

where c_θ^{s}, c_θ^{t} and c_θ^{c} are coefficients of the yield function in pure shear (s), pure tension (t) and pure compression (c) states, respectively, and m is material constant. In addition, the Lode angle dependency is mainly controlled by the parameter c_θ^{s}. It should be noted that the convexity condition of the modified yield condition can be found in Lian et al. (2013). Moreover, $f_p(T)$ is a temperature factor that describes the dependence of the yield stress on temperature, and $f_p(T)$ is defined as

$$f_p(T) = c_1 \exp^{-c_2 T}\,, \tag{6}$$

where T denotes the temperature in Kelvin.

The associate plastic flow is used, the plastic strain rate tensor can be computed as

$$\begin{aligned} \dot{\boldsymbol{\varepsilon}}^{\mathrm{pl}} &= \dot{\lambda}\frac{\partial g^{\mathrm{pl}}(\boldsymbol{\sigma})}{\partial \boldsymbol{\sigma}} \\ &= \dot{\lambda}\left\{ \frac{3}{2\sigma_{eq}}\mathrm{dev}\boldsymbol{\sigma} - \sigma_y\left[c_\theta^s + \left(c_\theta^{ax} - c_\theta^s\right)\left(\gamma - \frac{\gamma^{m+1}}{m+1}\right)\right]\right. \\ &\quad \times \frac{3\eta}{2\sigma_{eq}^2}\mathrm{dev}\boldsymbol{\sigma} - \sigma_y\left(c_\theta^{ax} - c_\theta^s\right)\left(1-\gamma^m\right) \\ &\quad \times \left(\frac{3\sqrt{3}}{2-\sqrt{3}}\right)\left(\frac{\tan(\theta-\pi/6)}{\cos(\theta-\pi/6)}\right)\frac{1}{\sigma_{eq}\sin 3\theta} \\ &\quad \left.\times\left(\frac{\mathbf{I}}{3} + \frac{\cos 3\theta}{2\sigma_{eq}}\mathrm{dev}\boldsymbol{\sigma} - \frac{3}{2\sigma_{eq}^2}\mathrm{dev}\boldsymbol{\sigma}\cdot\mathrm{dev}\boldsymbol{\sigma}\right)\right\} = \dot{\lambda}\mathbf{N} \end{aligned} \tag{7}$$

with

$$g^{\mathrm{pl}} = \sigma_{eq} - \sigma_y\left[c_\theta^s + (c_\theta^{ax} - c_\theta^s)\left(\beta - \frac{\beta^{m+1}}{m+1}\right)\right]\,, \tag{8}$$

where $\dot{\lambda}$ describes the non-negative plastic multiplier, $\mathbf{I}$ denotes the second-order identity tensor. It is noted that, as shown in Eq. (7), the plastic deformation does not contribute to the plastic dilatancy, as experimentally observed by Spitzig and Richmond (1984).

Furthermore, the isotropic Ludwik–Voce hardening law

$$\sigma_y = \rho\left[h_1 + h_2\cdot(\varepsilon^p)^{m_1}\right] + (1-\rho)\cdot\left[h_3(1 - h_4\cdot e^{m_2\varepsilon^p})\right] \tag{9}$$

is used to characterize plastic behavior, with the hardening moduli $\{h_1, h_2, h_3, h_4\}$, material constants $\{m_1, m_2, \rho\}$, and the equivalent plastic strain ε^p.

In addition, in the proposed model the damage is not initiated at the beginning, but is controlled by the damage initiation surface, which is different from the GTN model (Gurson, 1977), where no-damage surface exists and the damage initiates at the beginning accompanied with the plastic strain increments. The extended Johnson–Cook-type damage surface is defined as

$$\varepsilon_{\mathrm{ddi}}^p = (D_1 e^{-D_2\eta} - D_3 e^{-D_4\eta})\bar{\theta}^2 + D_3 e^{-D_4\eta}, \tag{10}$$

where $D_1 \ldots D_4$ are material parameters.

The damage evolution is governed by (Lian et al., 2013)

$$\dot{D} = \frac{\sigma_{d0}(\varepsilon_{\mathrm{df}}^p - \varepsilon_{\mathrm{ddi}}^p)}{G_f}\frac{\dot{\varepsilon}^p}{\varepsilon_{\mathrm{df}}^p} \tag{11}$$

where σ_{d0} denotes the stress value at the onset of damage, $\dot{\varepsilon}^p$ describes the equivalent plastic strain rate, and G_f is the energy required to open a unit area of crack.

3.3. Ductile and cleavage fracture model

In the proposed theory, ductile fracture is driven by the accumulation of the equivalent plastic strain, used as a scalar measure of plastic deformation. The fracture surface is defined analogously to the damage locus in Eq. (10). Similarly, the stress-state-dependent fracture locus is defined as

$$\varepsilon_{\mathrm{df}}^p = (F_1 e^{-F_2\eta} - F_3 e^{-F_4\eta})\bar{\theta}^2 + F_3 e^{-F_4\eta}, \tag{12}$$

with ductile fracture material parameters $F_1 \ldots F_4$.

For cleavage fracture under low temperatures, the strain-based ductile fracture surface is not suitable for capturing the fracture behavior. According to Ritchie (Ritchie et al., 1973), cleavage fracture is modeled by a critical stress. However, further studies (Kotrechko et al., 2007; Pineau, 2008) showed that the critical stress for cleavage fracture needs to consider the temperature effect. Thus, a modified Ritchie model considering both damage and temperature effects is proposed as

$$f^{\mathrm{bf}} = \sigma_1 - (1-D)\sigma_{1,y} f_b(T) \tag{13}$$

where $\sigma_{1,y} f_b(T)$ is the temperature-dependent first principal stress accounting for the temperature effect.

4. Numerical implementation

The elastic predictor–plastic corrector method with a single-step explicit forward Euler scheme is used to calculate the updated stress, the magnitude of plastic strain, and its direction. It is noted that the used methods assume that some parameters are unchanged and related to the initial conditions, and these values will be updated. Considering the interval from state n to $n+1$, the backward Euler method is used to discretize the constitutive equations as follows. All current variables with the subscript $n+1$ are omitted for better readability. The strain increment is assumed to be elastic, and the total elastic strain tensor is given by

$$\boldsymbol{\varepsilon}^{\mathrm{el,trial}} = \boldsymbol{\varepsilon}_n^{\mathrm{el}} + \Delta\boldsymbol{\varepsilon}\,. \tag{14}$$

Then, the trial value of the stress tensor, assuming no damage evolution, can be defined as

$$(1-D_n)\boldsymbol{\sigma}^{\mathrm{trial}} = (1-D_n)\boldsymbol{\sigma}_n + (1-D_n)\mathbb{C} : \Delta\boldsymbol{\varepsilon}\,, \tag{15}$$

where $\mathbb{C}$ denotes the fourth order elastic tangent modulus.

According to the consistency condition and the yield function, the increment of the equivalent plastic strain can be computed using the trial value in the form of

$$\Delta\lambda = \frac{(1-D_n)\sigma_{\mathrm{eq}}^{\mathrm{trial}} - \sigma_{\mathrm{threshold}}^{\mathrm{trial}}}{(1-D_n)(3G+H)} \tag{16}$$

with

$$\sigma_{\mathrm{eq}}^{\mathrm{trial}} = \sqrt{\tfrac{3}{2}\,\mathrm{dev}\boldsymbol{\sigma}^{\mathrm{trial}}\cdot\mathrm{dev}\boldsymbol{\sigma}^{\mathrm{trial}}} \tag{17}$$

and

$$\sigma_{\mathrm{threshold}}^{\mathrm{trial}} = (1-D_n)\sigma_y^{\mathrm{trial}} f_p(T)\left[c_\theta^s + (c_\theta^{ax} - c_\theta^s)\left(\beta - \frac{\beta^{m+1}}{m+1}\right)\right]\,, \tag{18}$$

where G describes the shear modulus and H denotes the hardening modulus.

Following Eq. (7), the stress direction is calculated in the form of

$$\begin{aligned}\mathbf{N} = &\frac{3}{2\sigma_{\text{eq}}^{\text{trial}}}\text{dev}\boldsymbol{\sigma} - \sigma_y^{\text{trial}}\left[c_\theta^s + \left(c_\theta^{ax} - c_\theta^s\right)\left(\gamma - \frac{\gamma^{m+1}}{m+1}\right)\right]\\ &\frac{3\eta}{2(\sigma_{\text{eq}}^{\text{trail}})^2}\text{dev}\boldsymbol{\sigma} - \sigma_y^{\text{trial}}\left(c_\theta^{ax} - c_\theta^s\right)(1-\gamma^m)\\ &\times\left(\frac{3\sqrt{3}}{2-\sqrt{3}}\right)\left(\frac{\tan(\theta-\pi/6)}{\cos(\theta-\pi/6)}\right)\frac{1}{\sigma_{\text{eq}}^{\text{trial}}\sin 3\theta}\\ &\times\left(\frac{\mathbf{I}}{3} + \frac{\cos 3\theta}{2\sigma_{\text{eq}}^{\text{trial}}}\text{dev}\boldsymbol{\sigma}^{\text{trial}} - \frac{3}{2(\sigma_{\text{eq}}^{\text{trail}})^2}\text{dev}\boldsymbol{\sigma}^{\text{trial}}\cdot\text{dev}\boldsymbol{\sigma}^{\text{trial}}\right).\end{aligned} \tag{19}$$

Using Eqs. (16) and (19), the increment of equivalent plastic strain can be calculated as

$$\Delta\varepsilon^{\text{p}} = \sqrt{\frac{2}{3}\Delta\boldsymbol{\varepsilon}^{\text{pl}}\cdot\Delta\boldsymbol{\varepsilon}^{\text{pl}}} = \sqrt{\frac{2}{3}\Delta\lambda\mathbf{N}\cdot\Delta\lambda\mathbf{N}} = \Delta\lambda\sqrt{\frac{2}{3}\mathbf{N}\cdot\mathbf{N}} \tag{20}$$

By combining Eqs. (11), (10), and (12), the damage variable can be updated based on the newly calculated $\Delta\varepsilon^{\text{p}}$ (20) as

$$D = D_n + \frac{\sigma_{d0}(\varepsilon_{\text{df}}^p - \varepsilon_{\text{ddi}}^p)}{G_f}\frac{\Delta\varepsilon^{\text{p}}}{\varepsilon_{\text{df}}^p}. \tag{21}$$

With the stress direction $\mathbf{N}$ and the plastic multiplier $\Delta\lambda$ in hands, the stress can be updated as

$$(1-D)\boldsymbol{\sigma} = (1-D)\,\mathbb{C} : \left(\boldsymbol{\varepsilon}^{\text{trial}} - \boldsymbol{\varepsilon}_n^p - \Delta\lambda\mathbf{N}\right). \tag{22}$$

The proposed continuum damage and fracture framework for characterizing the ductile-to-brittle transition is summarized in Algorithm 1. The constitutive model is implemented as a vectorized user material subroutine (VUMAT) in the commercial software Abaqus. The proposed subroutine is provided as supplementary material with this article.

Algorithm 1 Elastic–plastic–damage and fracture framework

History variables: $\mathfrak{S} \in \{\boldsymbol{\varepsilon}_n, \boldsymbol{\varepsilon}_n^{\text{el}}, \boldsymbol{\sigma}_n, \boldsymbol{\varepsilon}_n^{\text{pl}},\ D_n,\ D_{\text{ddi,n}}, \varepsilon_{\text{ddi}},\ D_{\text{df,n}}, \varepsilon_{\text{df}}\}$
Given strain field: $\boldsymbol{\varepsilon}^{\text{el,trial}} = \boldsymbol{\varepsilon}_n^{\text{el}} + \Delta\boldsymbol{\varepsilon}$
Compute and check the trial yield condition $f^{\text{pl,tri}}$
if $f^{\text{pl,tri}} > 0$ **then**
  Update $\boldsymbol{\varepsilon}^{\text{pl}} = \Delta\lambda\mathbf{N}$ using $\Delta\lambda$ (16) and $\mathbf{N}$ (19)
  Update damage and fracture indicator based on $\Delta\varepsilon^{\text{p}}$ (20):
    • Ductile damage indicator (DDI): $D_{\text{ddi}} = D_{\text{ddi,n}} + \frac{\Delta\varepsilon^{\text{p}}}{\varepsilon_{\text{ddi}}}$
    • Ductile fracture (DF): $D_{\text{df}} = D_{\text{df,n}} + \frac{\Delta\varepsilon^{\text{p}}}{\varepsilon_{\text{df}}}$
  Update D (21), $\boldsymbol{\varepsilon}^{\text{el}}$, and $\boldsymbol{\sigma}$ (22)
else
  Go to elastic part
  Update $\boldsymbol{\varepsilon}^{\text{el}}$ and $\boldsymbol{\sigma}$ (22)
end if
Check brittle fracture criterion
if $f^{\text{bf}} \geq 0$ (13) and $\varepsilon^p > \varepsilon_{\text{crit}}^p = 10^{-6}$ **then**
  Brittle Fracture occurs, Element Deletion Flag =0
end if
Check ductile fracture criterion
if $I_{\text{df}} \geq 1$ **then**
  Ductile Fracture occurs, Element Deletion Flag =0
end if

5. Identification of material parameters

This section describes the parameter identification strategy based on an experimental–numerical hybrid approach and its procedure. For the numerical simulations, C3D8R elements are used for all calculations. A mesh sensitivity study of the UT specimen shows that the results remain consistent within a mesh size range of 0.2 mm–0.5 mm. A mesh size of 0.4 mm, sufficient to capture plastic and damage behavior, is adopted for the UT specimen to reduce computational time. The other notched specimens require a finer mesh of approximately 0.2 mm. The details of the identified parameters and their validation are discussed in the following sections.

5.1. Overview of identification strategy

To incorporate the impact of loading history, the entire strain history as well as the evolution of stress state are extracted from the selected critical element in all simulation results. The stress state parameters are averaged with respect to the equivalent plastic strain, which are defined as

$$\eta_{\text{ave}} = \frac{1}{\varepsilon^p}\int_0^{\varepsilon^p}\eta\,\text{d}\varepsilon^p \quad\text{and}\quad \bar{\theta}_{\text{ave}} = \frac{1}{\varepsilon^p}\int_0^{\varepsilon^p}\bar{\theta}\,\text{d}\varepsilon^p. \tag{23}$$

According to the mean stress triaxiality η_{ave}, mean normalized Lode angle parameter $\bar{\theta}_{\text{ave}}$, and the corresponding equivalent plastic strain ε^p at ductile damage and fracture initiation, the respective damage and fracture loci can be calibrated using 3D curve fitting in MATLAB. This is achieved by finding the parameters $\mathbf{M} = \{D_1, D_2, D_3, D_4\}$ (10) and $\mathbf{M} = \{F_1, F_2, F_3, F_4\}$ (12) in the respective damage and fracture loci that minimize the following function

$$\mathbf{M} = \underset{\mathbf{M}}{\text{argmin}}\left(\frac{1}{N}\sum_{i=1}^{N}\left|\frac{\varepsilon^{p,\text{num}}(\eta_{\text{ave},i},\bar{\theta}_{\text{ave},i}) - \varepsilon^{p,\text{exp}}(\eta_{\text{ave},i},\bar{\theta}_{\text{ave},i})}{\varepsilon^{p,\text{exp}}(\eta_{\text{ave},i},\bar{\theta}_{\text{ave},i})}\right|\right), \tag{24}$$

where N represents the total number of fitting data points.

For cases where automatic fitting is challenging, the calibration of the damage locus can be simplified to a 2D situation, which is also practical for calibrating the ductile fracture locus. As seen in the modified Johnson–Cook-type locus (10), the influence of stress triaxiality η on the critical strain follows an exponential function, while the effect of the Lode angle parameter can be approximated by a quadratic function. Therefore, calibration at low Lode angle parameters is primarily controlled by D_3 and D_4, whereas D_1 and D_2 mainly influence calibration at high Lode angle parameters. The impact of D_1 and D_2 is relatively lower due to the quadratic nature of the Lode angle parameter function. This implies that at a high Lode angle parameter of 0.7, the contributions from $D_1 e^{-D_2\eta}$ and $D_3 e^{-D_4\eta}$ are nearly equivalent. However, achieving such an extremely high Lode angle parameter in practice is very difficult. From an experimental design perspective, at least three tests at different stress states with low Lode angle parameters and another three at high Lode angle parameters are required for a reliable calibration of the fracture locus. A similar approach can also be used to identify the fracture locus.

In addition, the damage softening behavior is mainly controlled by the parameter G_{f} (11) which represents the energy required to open a unit area of a crack. The softening equation is governed by

$$\Delta D = \frac{\sigma_{d0}(\varepsilon_{\text{df}}^p - \varepsilon_{\text{ddi}}^p)}{G_{\text{f}}}\frac{\Delta\varepsilon^p}{\varepsilon_{\text{df}}^p} = \frac{\sigma_{\text{d}}(\varepsilon_{\text{df}}^p - \varepsilon_{\text{ddi}}^p)}{G_{\text{f}}}\Delta D_{\text{df}}, \tag{25}$$

where ΔD represents the softening parameter in the incremental form of Eq. (11), and ΔD_{df} denotes the incremental of fracture indicator. As shown in Eq. (25), the softening behavior is also influenced by the ductile fracture strain. Specifically, an extremely high ductile fracture locus would be inappropriate when calibrating softening. Although the evolution of the ductile fracture indicator ΔD_{df} (25) is mathematically independent of the softening, the damage softening behavior significantly affects strain accumulation and influences the final ductile fracture. Thus, an iterative calibration strategy is recommended for softening and ductile fracture. First, an initial assumption of the ductile fracture locus is made based on the failure plastic strain observed in experiments. Then, the softening parameter G_{f} is inversely adjusted to ensure that the numerically predicted load–displacement curve agrees with the experimental results after damage initiation. Finally, after determining a suitable ductile fracture locus, the softening behavior should be rechecked for further optimization. The parameter identification strategy is additionally summarized in Fig. 3 as a flowchart.

It should be noted that there is no difference between the calibration strategy for the ductile fracture locus (12) and that for the ductile damage initiation locus (10). However, as a decisive step in the final

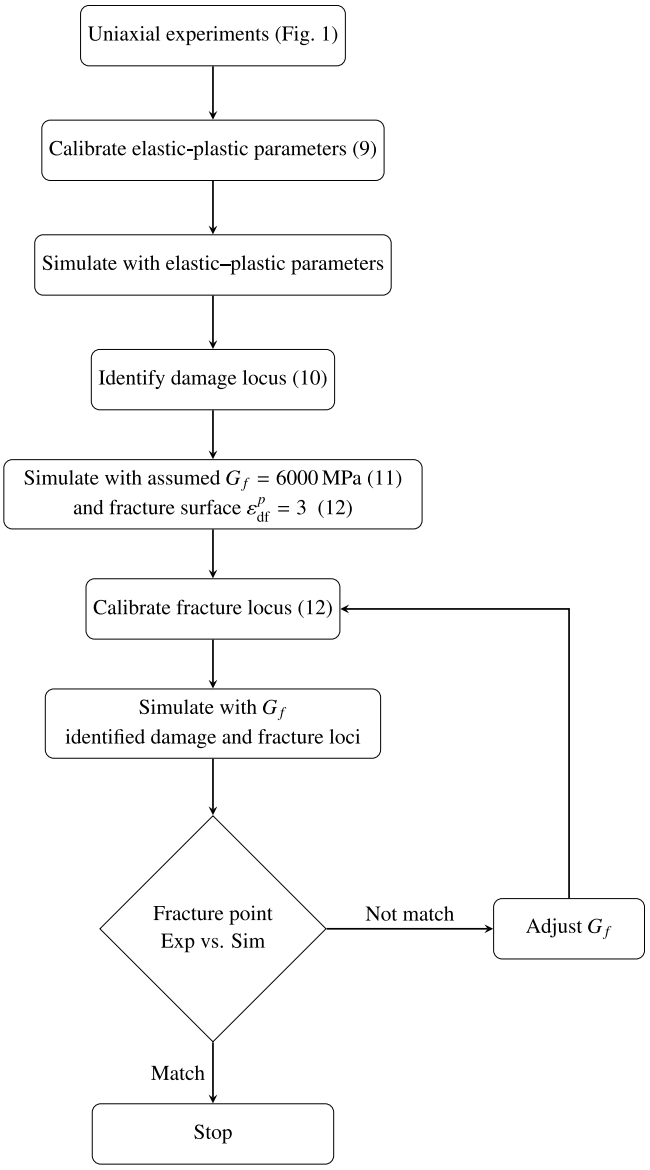


Fig. 3. Flowchart of the parameter identification strategy.

accuracy, calibration of material response, such as in the global load–displacement field, and local crack initiation and crack propagation path, greater attention should be given to ensuring good agreement between simulation and experiment.

5.2. Elastic–plastic results

Based on the experimental results of the uniaxial tension test, a nearly homogeneous stress state is generated in the region of interest (ROI) of the specimen before the onset of necking. The measured load–displacement curve can be converted into a true strain–true stress curve to identify mechanical properties, including Young's modulus and plasticity parameters. From the experimental results of the uniaxial tension (UT) test, Young's modulus of $E = 210000$ MPa and Poisson's ratio of $\nu = 0.25$ are determined. In addition, plastic parameters for the Ludwik–Voce hardening law in Eq. (9) can be directly calibrated using the least-squares curve fitting method. The parameter vector $\mathbf{x}$ should satisfy the following equation:

$$\min_{\mathbf{x}} \left\| \mathbf{F}(\mathbf{x}, \gamma_{\mathrm{data}}) - \sigma_{y,\mathrm{data}} \right\|_2^2 = \min_{\mathbf{x}} \sum_i (F(\mathbf{x}, \gamma_i) - \sigma_{y,i})^2 \quad \text{with} \quad \mathbf{x} = \{h_1, h_2, h_3, h_4, m_1, m_2, \rho\}, \tag{26}$$

where $\mathbf{F}(\mathbf{x}, \gamma_{\mathrm{data}})$ is a vector-valued function defined in Eq. (9), and the input vectors γ_{data} and $\sigma_{y,\mathrm{data}}$ are derived from experimental data measured from UT test.

In addition, deviations in yielding are observed in PSR3 and PSR15. The shape of the yield surface is further adjusted by modifying the parameter c^s_θ. At $c^s_\theta = 0.94$, $c^t_\theta = 1.00$, and $c^c_\theta = 0.99$, a satisfactory consistency is finally achieved between experimental results and numerical simulations. The identified elastic–plastic parameters are summarized in Table 2, and the corresponding experimentally measured and numerically predicted force–displacement curves for all geometries are presented in Fig. 4. It is evident that the simulated force–displacement curves agree well with the experimental results before the onset of ductile damage, particularly for elastic deformations and yield stresses. The difference between experimental and numerical results can be corrected by considering the damage effect.

Table 2
Elastoplastic parameters for the investigated high-strength steels S1100.

E [MPa]	ν [−]	c^s_θ [−]	c^t_θ [−]	c^c_θ [−]	ρ [−]
210 000	0.25	0.94	1.00	0.99	0.52
h_1 [MPa]	h_2 [MPa]	m_1 [−]	h_3 [MPa]	h_4 [MPa]	m_2 [MPa]
3209	8278	0.03	12 883	1.63	0.02

5.3. Ductile damage and fracture results

By comparing the numerically predicted load–displacement curves without damage to the experimental ones, shown as blue curves, the corresponding ductile damage initiation points are marked with blue circles in Fig. 4. The element with the maximum equivalent plastic strain ε^p at the ductile damage initiation step is directly identified as the critical element. The strain history and stress state of these critical elements are extracted and integrated to determine the mean stress states η_{ave} and θ_{ave} (23). It is evident that the equivalent plastic strains at damage initiation $\varepsilon^p_{\mathrm{ddi}}$ differ only slightly between different loading cases. Based on the obtained stress state variables and corresponding equivalent plastic strains, as summarized in Table 3, the ductile damage initiation locus can be directly fitted using 3D curve fitting in MATLAB using Eq. (24). The calibrated parameters and damage locus are presented in Fig. 5(a).

The softening parameter used in the characterization of the evolution of damage (25) is initially estimated as $G_{\mathrm{f}} = 6000$ MPa, which provides a reasonable approximation for a constant ductile fracture value of $\varepsilon^p_{\mathrm{df}} = 3$. This constant ductile fracture locus is achieved by setting the parameters as $F_1 = F_3 = 3$ and $F_2 = F_4 = 0$ in Eq. (12). Based on the above-mentioned $G_{\mathrm{f}} = 3000$ MPa and assumed fracture surface, the numerically predicted equivalent plastic strains are observed either at the middle of the notched section or at the edge of the notches, as illustrated in Fig. 6. Thus, strain history and stress state data with mechanical softening are re-extracted and used to calibrate the ductile fracture locus, which is listed in Table 3. Furthermore, the plane strain tests (PSR3 and PSR15) exhibit the lowest maximum plastic strain values due to the significantly high stress triaxialities generated, whereas the CE experiment shows the highest fracture strain among others, with minimal triaxiality. It should be noted that the critical element position for the CH specimen does not correspond to the location of the maximum equivalent plastic strain $\varepsilon^p = 0.95$, as depicted in Fig. 6(c). Instead, the critical element is defined as the element where the maximum fracture indicator $D_{\mathrm{df}} = 1.0$ occurs, as shown in Fig. 7(b). Additionally, as observed in Fig. 7(c), the stress

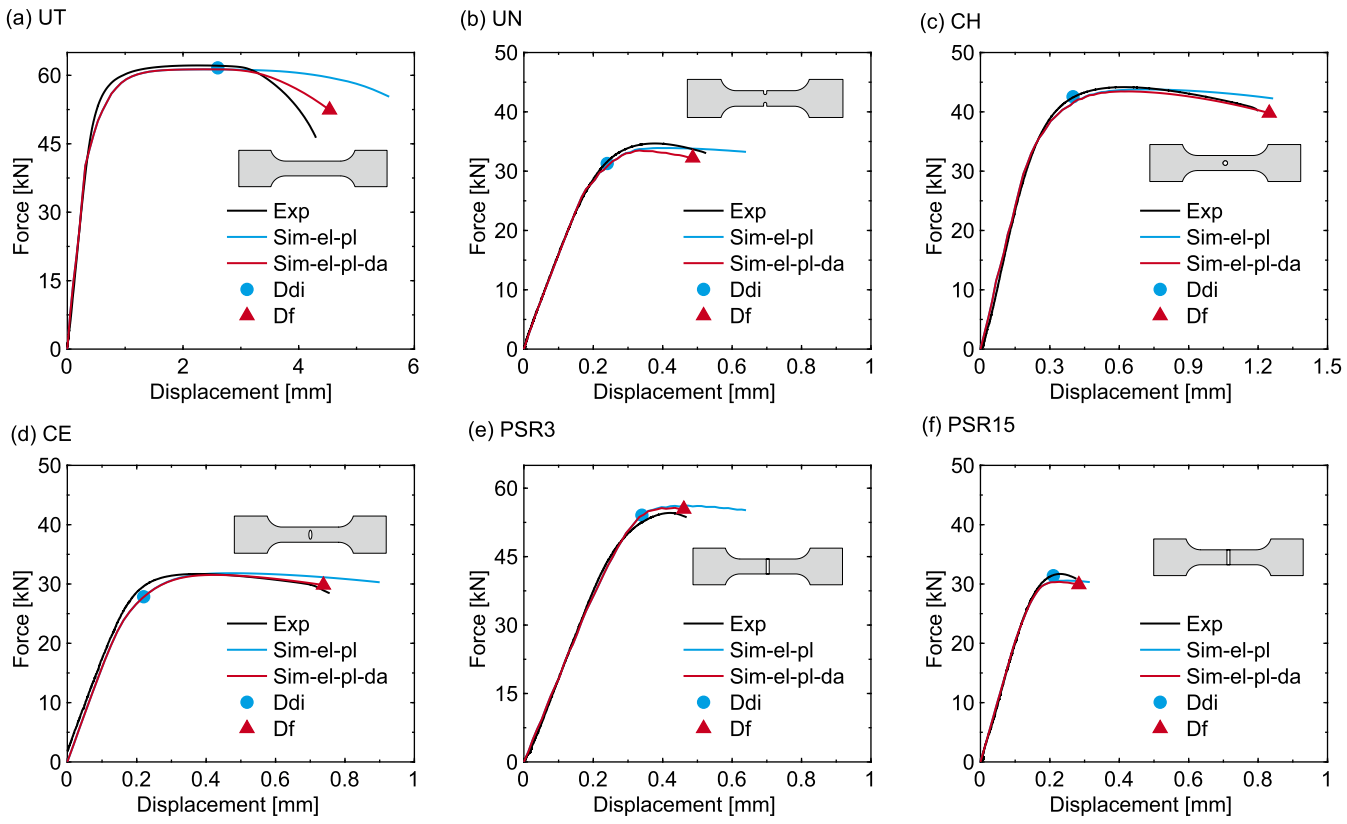


Fig. 4. Numerically predicted and experimentally measured load–displacement curves. Blue curves represent the numerical results obtained using the elastic–plastic model (without damage), and red curves correspond to the elastic–plastic-damage model.

Table 3
Stress state variables and respective plastic strains for the critical elements.

Tests	Calibrated damage initiation			Calibrated fracture initiation			Simulated fracture points		
	η_{ave}	$\bar{\theta}_{ave}$	ε^p_{ddi}	η_{ave}	$\bar{\theta}_{ave}$	ε^p_{df}	η_{ave}	$\bar{\theta}_{ave}$	ε^p_{df}
UT	0.33	1.00	0.04	0.72	0.35	0.78	0.72	0.35	0.39
UN	0.35	0.96	0.04	0.67	0.07	0.20	0.67	0.07	0.17
CH	0.34	0.98	0.10	0.80	0.36	0.59	0.80	0.36	0.38
CE	0.42	0.90	0.09	0.59	0.42	1.11	0.59	0.42	0.52
PSR3	0.76	0.17	0.03	0.84	0.01	0.14	0.84	0.01	0.11
PSR15	0.61	0.06	0.05	0.67	0.01	0.18	0.67	0.01	0.16

triaxiality at this position is also significantly higher than at the location of maximum plastic strain.

For a more accurate calibration for the fracture locus, the fracture strain ε^p_{df} data are divided into high Lode angle parameter and low Lode angle parameter groups. As summarized in Table 3, the UN, PSR3, and PSR15 experiments exhibit significantly smaller Lode angle parameters than the UT, CH, and CE experiments. Therefore, experiments with low Lode angle parameters are used to identify F_3 and F_4, since the fracture strain is mainly affected by stress triaxiality in Eq. (12). Conversely, F_1 and F_2 are calibrated using experiments with high Lode angle parameters, including those from UT, CH, and CE. Fig. 5(b) shows the identified fracture locus and respective parameters. Subsequently, the softening parameter was adjusted to $G_f = 3000$ MPa. With smaller G_f values, the mechanical softening becomes more pronounced, increasing from 5% to 10%. The resulting numerically predicted force–displacement curves, considering damage and fracture, are shown as red curves in Fig. 4. It can be observed that the numerical load–displacement curves align well with the experimental results, including damage softening and the fracture point.

For further assessment of the calibration accuracy, the respective strain path is extracted, as illustrated in Fig. 8(a). It is observed that the stress triaxiality and Lode angle parameter for the critical elements change significantly during the loading process. For example, the normalized Lode angle parameter $\bar{\theta}$ changes from 1 to nearly 0 for plane strain experiments and from 0.9 to 0.4 for the CE test. The fracture locus defines the critical plastic strain for each stress state; however, ductile fracture does not necessarily occur when the accumulated plastic strain reaches the critical strain surface. For the proposed model, the loading history dependency is incorporated by introducing an indicator $\Delta D_{df} = \frac{\Delta\varepsilon^p}{\varepsilon^p_{df}}$ recording the accumulation of ductile fracture rather than direct comparing plastic strain with critical value. Briefly speaking, each loading step generates a different stress state. Therefore, based on the stress state, a corresponding fracture strain can be identified from the fracture locus. Using the current plastic strain increment and the fracture strain, the contribution of the current plastic strain increment can be computed and accumulated throughout the loading process. When this ductile fracture indicator D_{df} reaches a value of one, the element will be deleted. Although element deletion is solely governed by this indicator, the approach does not directly yield the final calibrated ductile fracture locus, as fracture does not necessarily occur when the strain reaches its critical value.

Taking the strain history into account, a normalized equivalent strain parameter ε^p_{norm} is introduced in this research. The mathematical

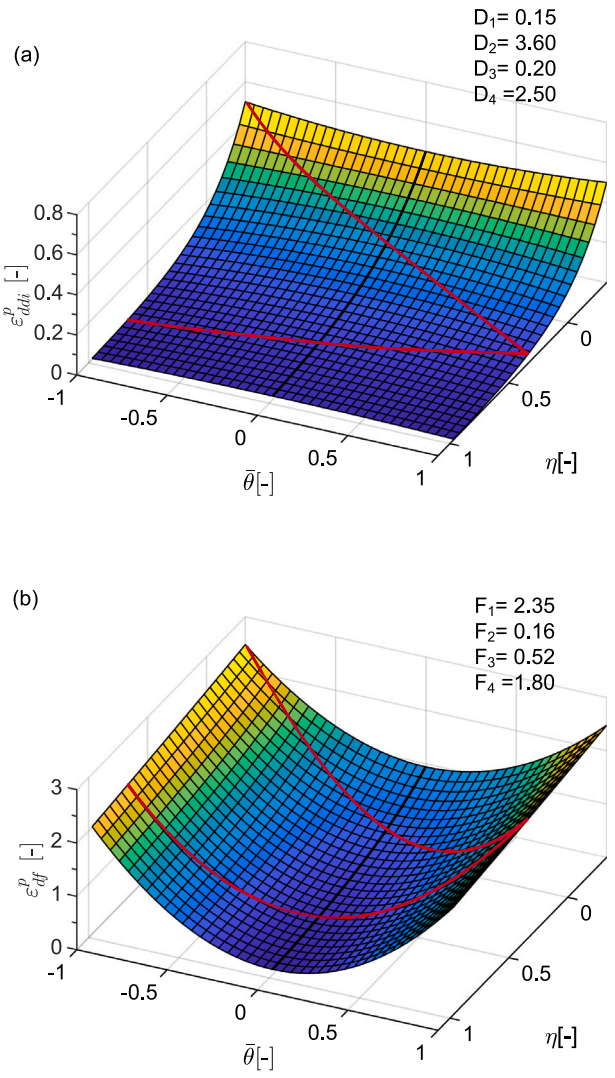


Fig. 5. Calibrated damage locus (a) and fracture locus (b).

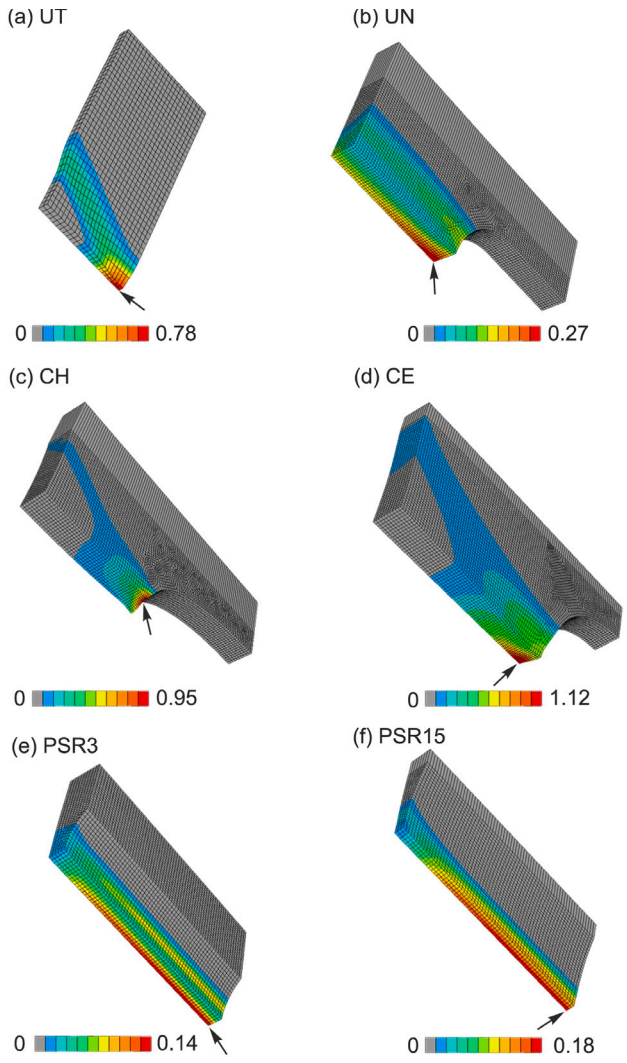


Fig. 6. Numerically predicted the equivalent plastic strains ε^p in the critical positions. A small arrow indicates the location of the critical element.

expression is given by

$$\begin{aligned}\varepsilon^p_{\text{norm}} &= \Delta\varepsilon^p \frac{\varepsilon^p_{\text{df}}}{\frac{1}{2}(\varepsilon^p_{\text{df}} + \varepsilon^p_{\text{df},n})} + \varepsilon^p_{\text{norm},n}\frac{\varepsilon^p_{\text{df}}}{\varepsilon^p_{\text{df},n}} \\ &= \Delta D_{\text{df}}\varepsilon^p_{\text{df}} + D_{\text{df},n}\varepsilon^p_{\text{df}},\end{aligned} \tag{27}$$

where $\varepsilon^p_{\text{df},n}$ is the critical plastic strain of ductile fracture at time step n which is calculated from the stress state (η_n and θ_n) from the last step by applying the calibrated ductile fracture parameters. $\Delta\varepsilon^p$ stands for the current equivalent plastic strain increment, which is normalized by the average critical plastic strain within this increment since the midpoint approach is used to ensure more stable results. Both $\Delta\varepsilon^p$ and $\varepsilon^p_{\text{df},n}$ are normalized as a respective rate ΔD_{df} and $D_{\text{df},n}$ mapped to the current stress state. The critical plastic strain of this updated stress state is denoted as $\varepsilon^p_{\text{norm}}$. With the introduction of this equivalent value, the strain path can be extracted and projected into two 2D plots. The fracture locus is also projected with limiting stress state value. The damage evolution approaching the damage surface can then be clear, as shown in Fig. 8.

6. Ductile-to-brittle transition behaviors

This section compares the numerical results with the experimental observations in terms of the global force–displacement curves, impact energy, and the evolution of strain and stress states. A detailed analysis of the different fracture mechanisms, based on the numerical simulations, is conducted at the element level. Finally, the SEM observations and fracture profiles are presented and discussed in detail.

6.1. Force–displacement and impact energy

In this work, the full sub-sized Charpy specimen was simulated in Abaqus using 147,254 brick elements with reduced integration (C3D8R), with a fine mesh of 0.2 mm in the V-notch region, where fracture is expected to occur. Only half of the simulation model is shown in Fig. 9(a). The anvil and striker are set as rigid bodies; therefore, only coarse meshes are used for these components, as shown in Fig. 9(a). In addition, a fine mesh is defined in the V-notch region, where damage and fracture are expected to occur, and the details of the V-notch cross-section are illustrated in Fig. 9(b). In the numerical simulations, a quasi-static loading condition was applied. Within the proposed framework, the strain rate is assumed to affect only the plastic yield point, while its influence on damage evolution and fracture initiation is neglected. Since the present study focuses primarily on fracture initiation, the quasi-static loading assumption is therefore appropriate. In addition, during the numerical simulation, the friction coefficient

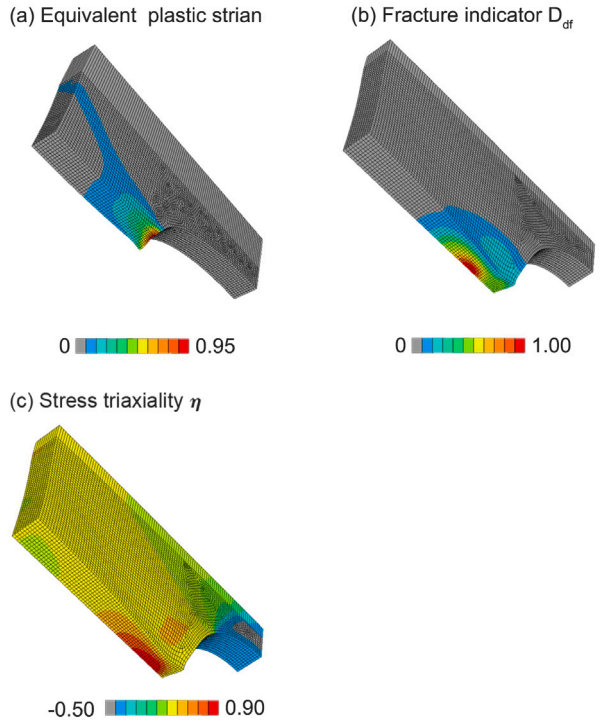


Fig. 7. Numerically predicted the equivalent plastic strain, the fracture indicator D_{df} and the stress triaxiality η in the critical position for the central hole (CH) experiment.

was set to 0.1. For the temperature-dependent brittle fracture criterion given in Eq. (13)

$$\sigma_{1,y} f_b(T) = \begin{cases} 3000 + 0.06076\,(T-77)^2 & T \le 178\ \text{K}, \\ 3918 - 1.645\,T, & T > 178\ \text{K} \end{cases}, \tag{28}$$

the parameters were inversely identified by fitting the simulated and experimental Charpy force–displacement curves obtained at −196 °C (corresponding to 77 K), −92 °C (approximately 178 K), and room temperature. It must be emphasized that the Charpy tests at the remaining 11 temperatures were not used for parameter identification but served as validation cases to verify the identified critical principal stress for brittle fracture.

The force–displacement curves for the sub-sized Charpy tests under different temperatures are shown in Fig. 10. It is evident that the experimental curves agree well with the numerical results in terms of the maximum force and the fracture initiation points. The maximum simulated force $F_{\text{sim,max}}$ agrees well with the experimental value $F_{\text{exp,max}}$ within 5%, and the relative mean error between experiments and simulations is only 2.11%, indicating very good agreement between the experimental results and numerical predictions using the present constitutive model. In addition, the maximum force first shows an increasing trend with decreasing temperature, rising from $F_{\text{exp,max}}$ = 9.99 kN at 23 °C to $F_{\text{exp,max}}$ = 11.25 kN at −115 °C. It then decreases to $F_{\text{exp,max}}$ = 7.94 kN at −196 °C. Moreover, one can also observe that, with decreasing temperature from room temperature to −196 °C, the post-peak force decreases more rapidly, indicating an increase in the brittleness of the material behavior with decreasing temperature. At −92 °C, no zigzag force–displacement behavior is observed, indicating brittle fracture behavior.

The total energy E_{m} measured from the dial of the Charpy testing device and the numerically calculated energy E_{sim} are plotted in Fig. 11. The data are fitted using the hyperbolic tangent function proposed by (Oldfield, 1979):

$$E = A + B\tanh\left(\frac{T+C}{D}\right), \tag{29}$$

where A = 10.64, B = 11.26, C = −110.15, and D = 87.45. It is obvious that the numerically predicted energy E_{sim} agrees well with the experimentally measured energy E_{m}, and the scatter of the data around the fitted curve remains within the $\pm 1.5\sigma$ confidence interval, indicating high fitting accuracy and consistent model performance (approximately 86% confidence level). This finding confirms that the proposed continuum damage and fracture framework can effectively and accurately characterize the sub-sized Charpy experiments.

6.2. Stress states, plastic strains and damage evolution

The stress states at different cut planes of the sub-sized Charpy specimen, taken just before the rapid force drop predicted in the simulation, are shown in Fig. 12 for four representative temperatures. The stress triaxialities and normalized Lode angle parameters vary only slightly with temperature. The stress triaxiality distribution over the notch cross-section (plane 1) is non-uniform, exhibiting positive stress states in the upper region and negative stress states in the lower region. A pronounced localization is observed at the top of the notch, with a maximum value of approximately $\eta = 1.2$, as shown in Fig. 12(a1–d1), corresponding to a normalized Lode angle parameter of $\bar{\theta} = 0$. In addition, beyond plane 2 (see Fig. 12(e)), which is located approximately 5 mm from the V-notch (plane 1), the stress state becomes more homogeneous since no significant plastic deformation occurs in this region. These findings indicate that temperature variation only slightly affects the stress states when using the same testing specimen. Non-homogeneous stress distributions are generated due to the presence of the V-notch, which coincides with the expected fracture region.

In addition, the distributions of the first principal stress σ_1, the equivalent plastic strain ε^p, and the damage variable D at the four selected temperatures are illustrated in Fig. 13, respectively. From room temperature (25 °C) down to −92 °C, the distributions of the maximum values of σ_1, ε^{P}, and D appear similar in the notched cross-section (plane 1). At −196 °C, the maximum principal stress and equivalent plastic strain are localized at the top of the notch cross-section, as shown in Fig. 13(d1). Moreover, no damage occurs at −196 °C, since the plastic strain remains very small and does not reach the initiation threshold.

The stress triaxiality and the corresponding evolution of the equivalent plastic strain ε^p and the damage variable D, extracted from the critical element at the onset of force drop, are shown in Fig. 14. It can be observed that the evolution can be approximately divided into four distinct clusters. At −196 °C, the smallest damage evolution is observed, with $\varepsilon^p = 0.008$ and $D = 0.035$. The temperatures ranging from 25 °C to −69 °C belong to one cluster, which exhibits maximum values of approximately $\varepsilon^p = 0.7$ and $D = 0.3$. Compared with this cluster, the second cluster, containing the temperatures −82 °C, −92 °C, and −100 °C, shows similar maximum values of ε^p and D. However, the maximum stress triaxiality is only $\eta \approx 0.35$, which is lower than that of the first cluster ($\eta \approx 0.8$). In addition, the sub-sized specimens tested at −115 °C, −125 °C, and −145 °C exhibit similar evolution paths. Only the critical elements under −125 °C and −145 °C experience fracture, characterized by relatively low stress triaxiality values as well as small equivalent plastic strain and damage levels. The analysis of the evolution of the equivalent plastic strain and damage under different temperatures indicates that temperature variations significantly influence plasticity, damage, and fracture behavior. However, when the temperature remains within a certain range, this influence becomes relatively minor.

6.3. Ductile and brittle fracture behaviors

The fracture surfaces at the four selected temperatures are shown in Fig. 15. Different colors represent different fracture modes: green elements indicate brittle fracture, where elements are deleted after activation of the brittle fracture criterion; yellow elements represent

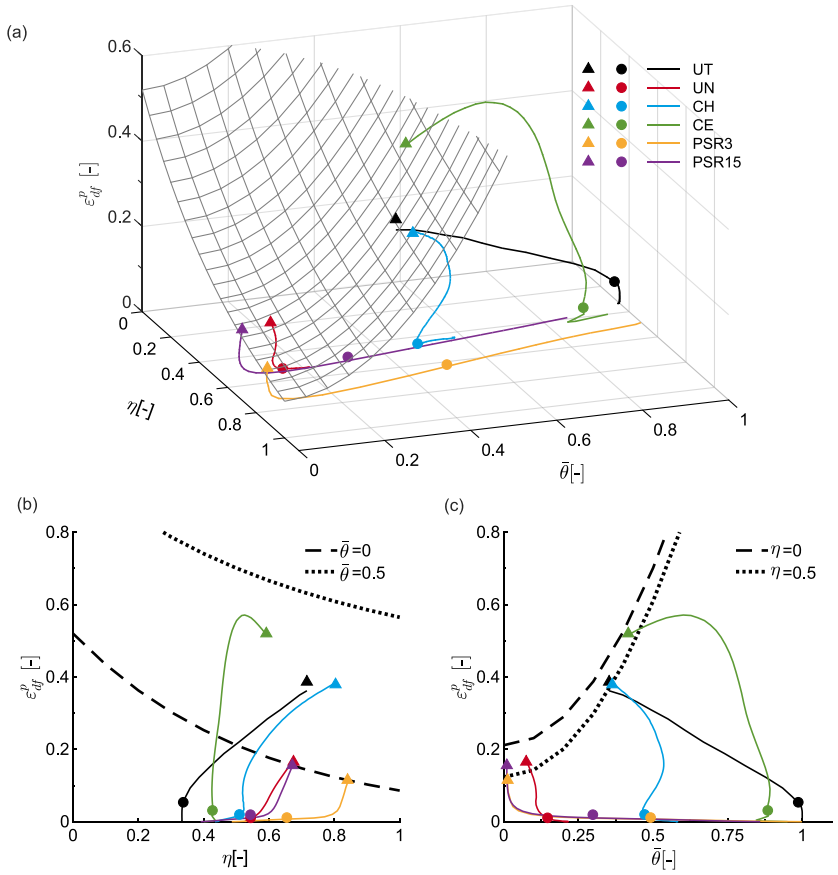


Fig. 8. Evolution of stress state dependent fracture strain ϵ^p_{df} (a) and its projection in strain-stress triaxiality space (b) and strain-Lode angle parameter space (c). Note that the location of the critical element is shown in Fig. 6.

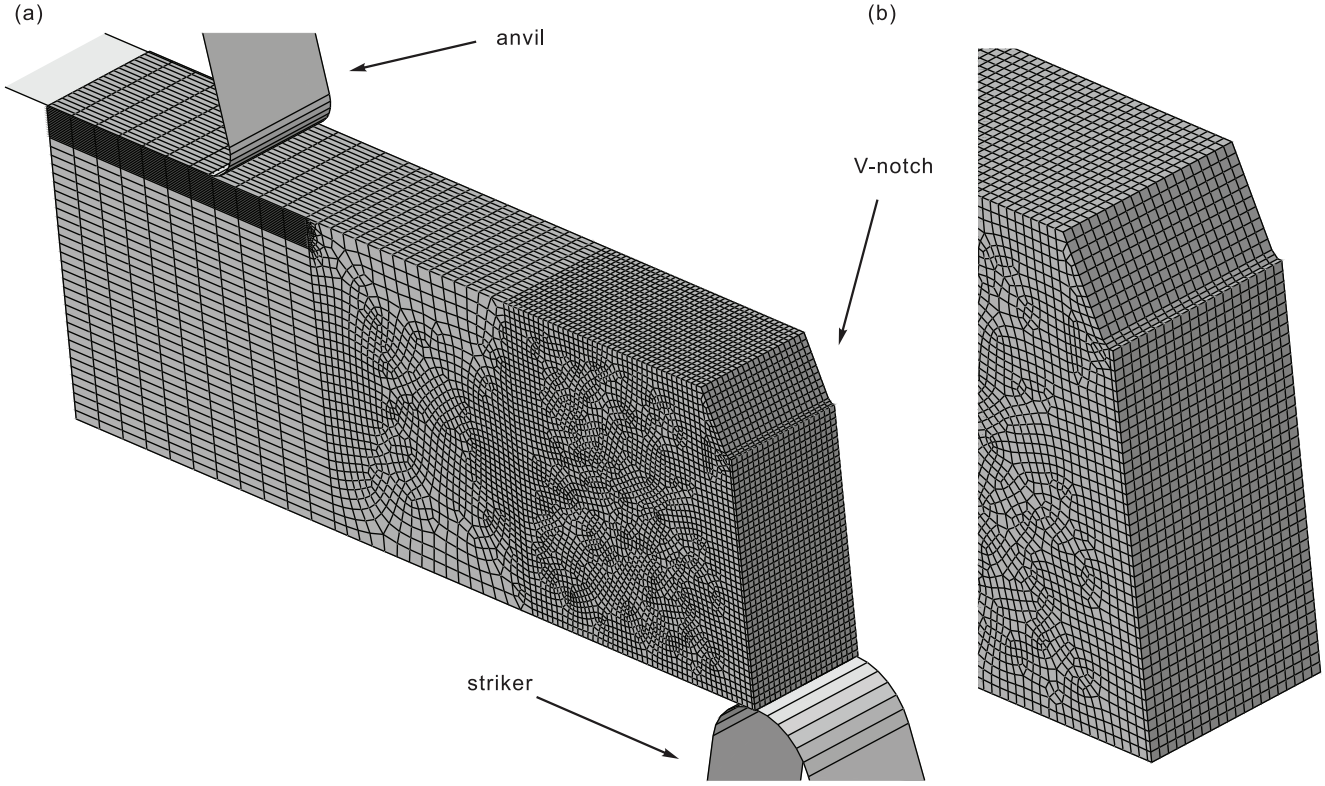


Fig. 9. (a) Overview of the sub-sized Charpy specimen and (b) detailed view of the V-notch cross-section.

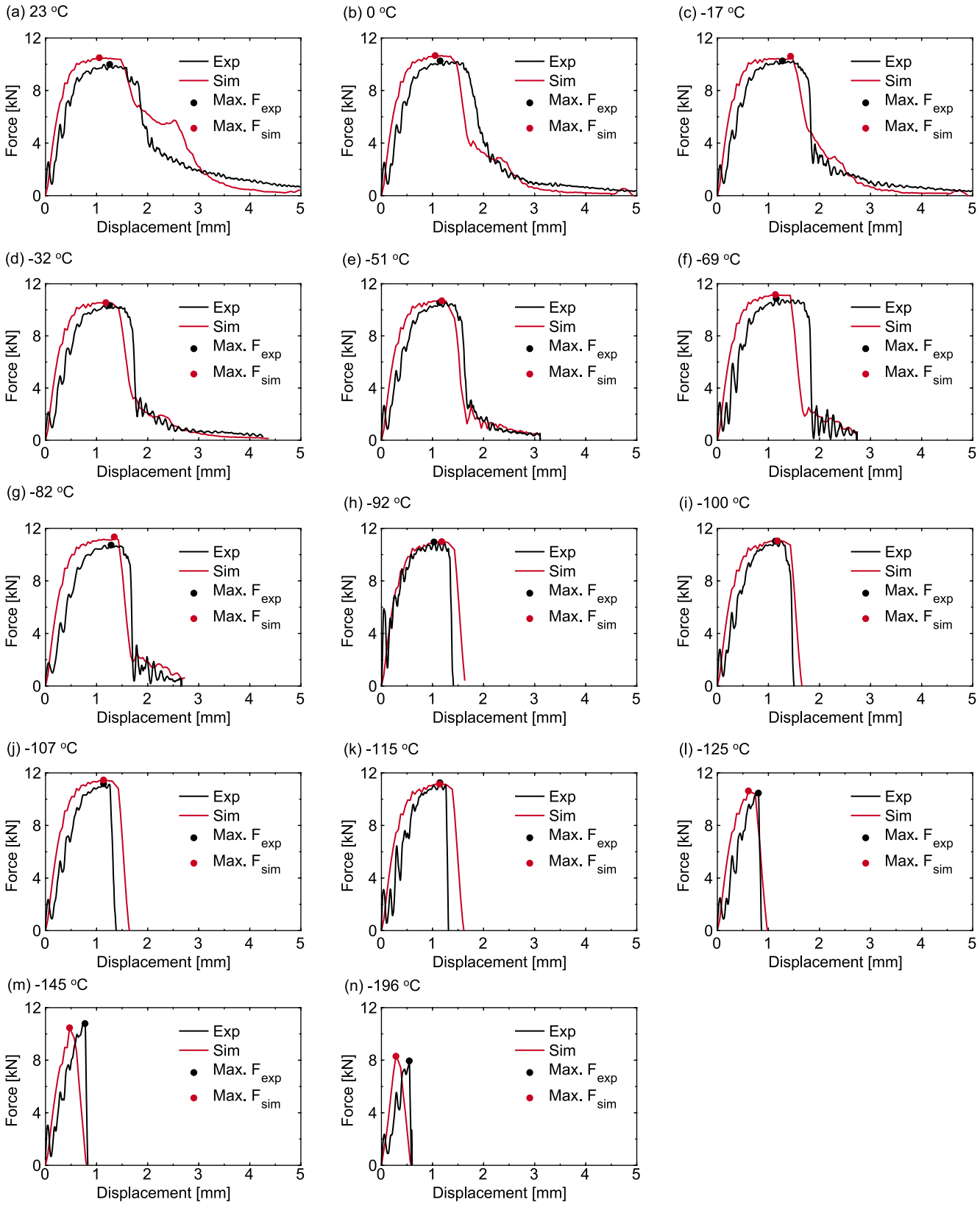


Fig. 10. Numerically predicted and experimentally measured load–displacement curves for sub-size Charpy test under different temperatures. The experimental curves in subfigures (a), (h), and (n) are employed for inverse fitting of the temperature-dependent brittle fracture criterion in Eq. (28).

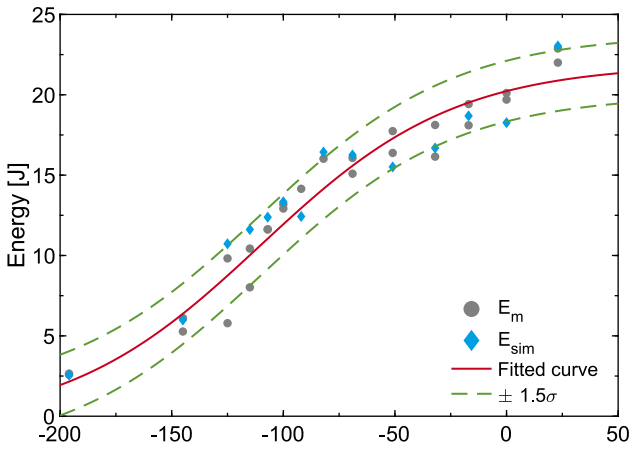


Fig. 11. Comparison of the experimentally measured and numerically predicted total impact energy.

regions experiencing damage evolution and material degradation due to the progression of ductile damage; and red elements correspond to regions that have reached the ductile fracture condition. It is evident that the fracture surface at room temperature (25 °C) is significantly rougher than those at lower temperatures. In contrast, the fracture surface at −196 °C appears markedly flatter and smoother, indicating a typical brittle fracture morphology. Brittle fracture contributes to all temperature conditions; however, it increases as the temperature decreases, consistent with the trend observed in the force–displacement curves shown in Fig. 10. It is noted that, as observed in the force–displacement curves, the force drops rapidly once the fracture point is reached, followed by a more gradual decrease in force indicating ductile behavior, as illustrated in Fig. 10(a)–(g). This behavior is attributed to brittle fracture, as also predicted numerically in Fig. 15. These results indicate that, under Charpy impact conditions, the investigated high-strength steel exhibits partial brittle fracture even at room temperature; however, it is not the dominant fracture mode, as can be seen by comparing Fig. 15(a2) and (a4), where the number of elements associated with brittle and ductile damage is approximately 366 and 328, respectively. It should be noted that the reported numbers of elements correspond to the complete Charpy specimen, whereas Fig. 15 shows only half of the geometry. For the sub-sized samples tested at −82 °C and −92 °C, the numbers of brittle and ductile elements are 534 and 275, and 568 and 244, respectively. This reveals that the proportion of brittle fracture increases while the ductile contribution decreases with decreasing temperature. This trend becomes even more evident at −196 °C, where 375 elements exhibit brittle fracture and only 25 elements show ductile damage. In addition, the number of elements exhibiting damage initiation and evolution decreases significantly with decreasing temperature. This is because brittle fracture, which is associated with relatively small values of equivalent plastic strain, may not activate the damage surface. Moreover, the statistical analysis of the three different types of elements, including those with deletions caused by brittle and ductile fractures, as well as elements with damage histories, for all temperatures, is plotted in Fig. 16. As shown in Fig. 16(a), the number of elements deleted due to active ductile and brittle fracture is presented, together with the ratio of brittle to total fractured elements. A clear trend can be observed: as temperature increases, the number of elements deleted due to brittle fracture decreases, while those associated with ductile fracture increase. At −52 °C and −69 °C, a balance between brittle and ductile fracture is reached. Moreover, the ratio of brittle to total fractured elements decreases with increasing temperature, reaching approximately 53% at −52 °C and −69 °C.

The number of elements affected by the occurrence and evolution of damage increases significantly with rising temperature. A pronounced change is observed between −125 °C and −115 °C, where the number of affected elements increases from 3324 to 5501. Since ductile fracture occurs when the damage and plastic strain reach the ductile fracture criterion, the corresponding elements are subsequently deleted. The ratio of elements deleted due to ductile fracture to the total number of elements affected by damage and ductile fracture is also shown in Fig. 16(b). The maximum ratio, approximately 7%, is observed at room temperature (25 °C), whereas below −69 °C, this ratio decreases to less than 4%. The above numerical analysis of brittle fracture, damage, and ductile fracture clearly reveals the differences in the occurrence and evolution of damage and fracture behavior in the Charpy tests conducted at different temperatures. These findings also highlight that the proposed material model can effectively capture the ductile-to-brittle transition behavior.

In addition, a comparison of the brittle and ductile fracture behavior for the Charpy tests at 25 °C and −82 °C is presented in Fig. 16(c) and (d), respectively. It is worth noting that the corresponding sections of the force–displacement curves after crack initiation for these two temperatures are extracted from the global curves shown in Fig. 10(a) and (g). Interestingly, between displacements of 1.4 and 1.7 mm, marked as points A and B, the number of brittle fractured elements rapidly increases from 0 to 141, exceeding the 136 ductile fracture elements. This clearly indicates that brittle behavior strongly contributes to the sudden force drop. Furthermore, between points C and D, the force decreases sharply again, accompanied by a significant increase in brittle elements from 148 to 215. The contribution of brittle fracture to the significant force drop can also be identified by comparing the force–displacement curve between points E and F, where a pronounced increase in brittle fracture is numerically predicted. These observations highlight the contribution of brittle fracture to the significant and rapid force drop. The evolution trends of brittle and ductile fracture also differ from each other, as numerically observed at room temperature.

6.4. Fracture pictures and SEM images

The cracks in the sub-sized Charpy specimens are shown in Fig. 17, and the corresponding fracture surfaces were examined using SEM. The respective SEM images are presented in Fig. 18. It can be observed that the fracture lines become straighter with decreasing temperature, from room temperature (25 °C) down to −196 °C. Typical cup-and-cone-type fracture surfaces are visible up to approximately −52 °C. For the fracture surface obtained from the sample tested at room temperature (25 °C), three different positions are shown in Fig. 18(a1)–(a3). Numerous micro-voids and large coalesced voids can be observed, indicating pronounced ductile deformation. However, Fig. 18(a2) and (a3), which were taken from the same fracture surface but at different locations, clearly reveal regions of brittle fracture, particularly in Fig. 18(a3). Moreover, the experimentally measured and numerically predicted impact energies at room temperature, illustrated in Fig. 11, suggest that 25 °C may not yet have reached the upper-shelf impact energy, implying that the fracture behavior at this temperature is not fully dominated by ductile fracture. Moreover, as observed in the global force–displacement curve, a sudden drop in force can be seen in Fig. 10(a), which is caused by the sudden activation of brittle fracture, as discussed in Fig. 16. These observations indicate that, at room temperature, the Charpy test for the investigated high-strength steel exhibits partial brittle fracture behavior in certain regions, while ductile fracture remains dominant. This conclusion is further supported by the numerical simulations, where the analysis of deleted elements associated with brittle and ductile fracture confirms that ductile damage predominates, although brittle fracture also occurs locally.

In addition, micro-voids and cleavage can be observed on the fracture surfaces at −51 °C and −92 °C, as shown in Fig. 18(b) and (c), respectively. Larger micro-voids are visible at −51 °C in Fig. 18(b) compared to those at −92 °C. This observation is consistent with the global

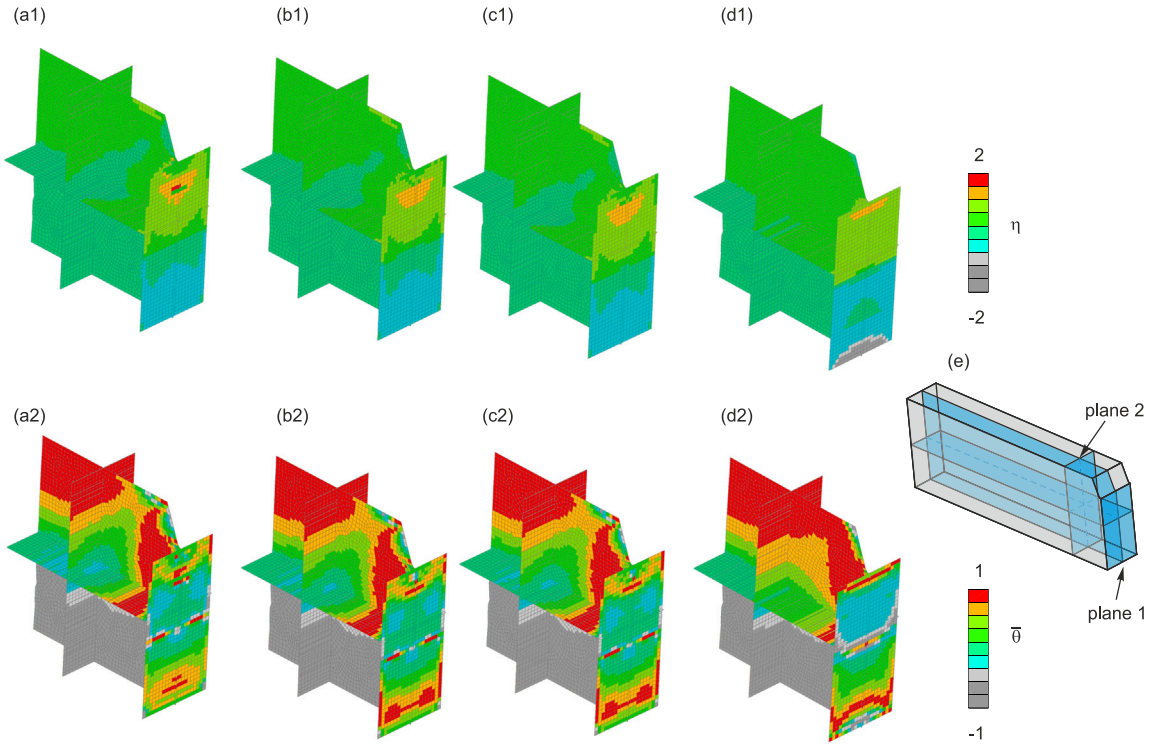


Fig. 12. Distribution of stress triaxiality η (a1–d1) and normalized Lode angle parameter $\bar{\theta}$ (a2–d2) at different cut planes: (a1–a2) 25 °C, (b1–b2) −82 °C, (c1–c2) −92 °C, (d1–d2) −196 °C, and (e) schematic illustration of the cut-plane orientation within the sub-sized Charpy specimen.

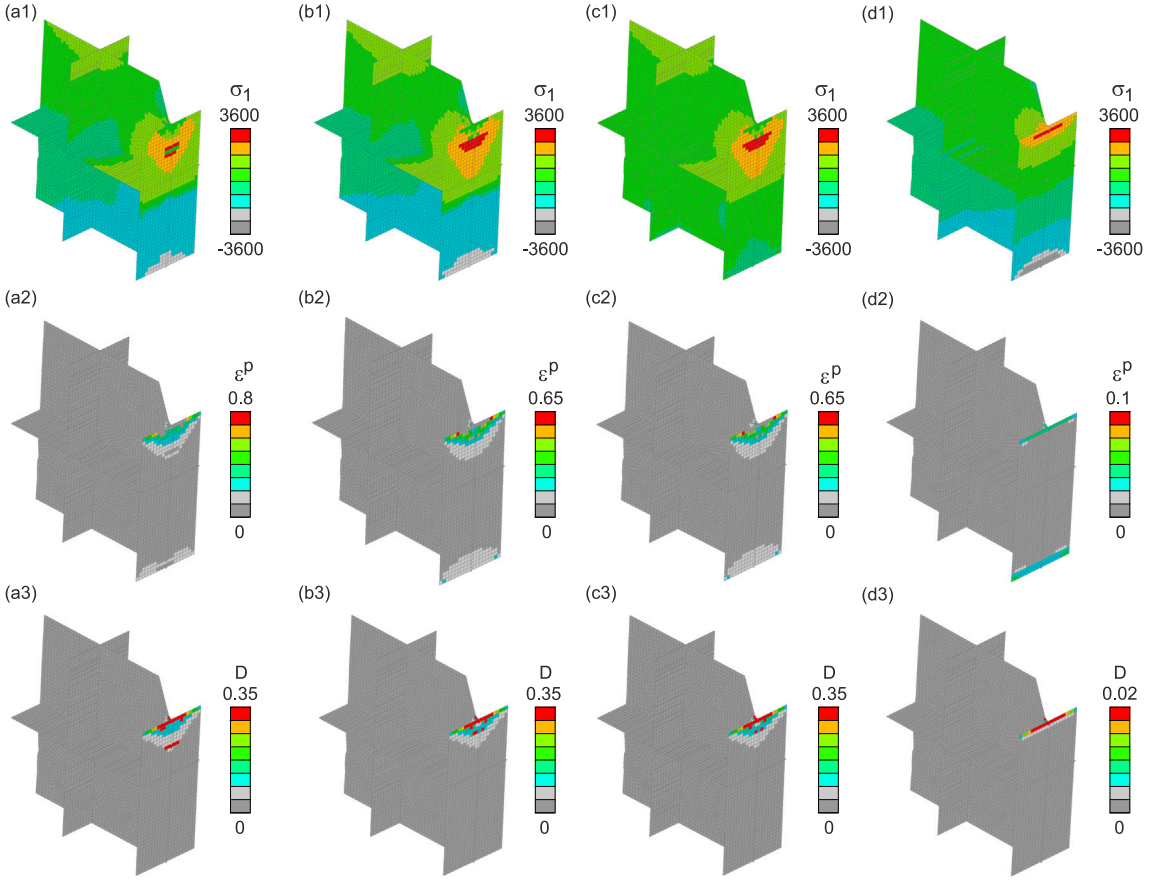


Fig. 13. Distribution of the first principal stress σ_1 (a1–d1), the equivalent plastic strain ε^p (a2–d2) and the damage variable D (a3–d3) at different cut planes: (a1–a3) 25 °C, (b1–b3) −82 °C, (c1–c3) −92 °C, and (d1–d3) −196 °C.

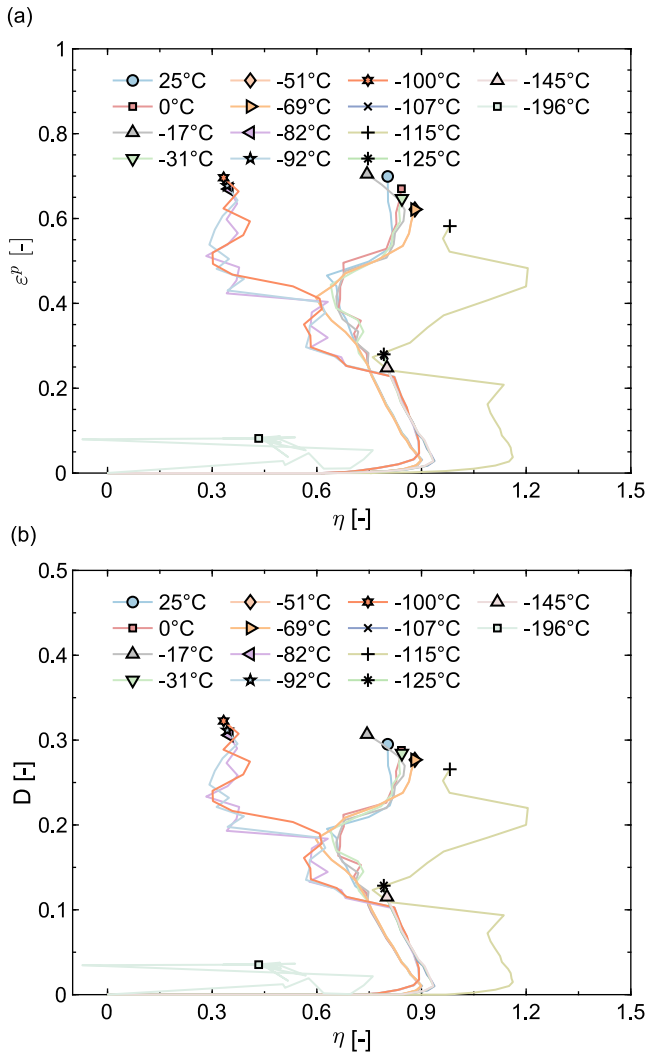


Fig. 14. Evolution of stress triaxiality η with equivalent plastic strain ϵ^p and damage variable D for the critical elements at 14 different temperatures, respectively.

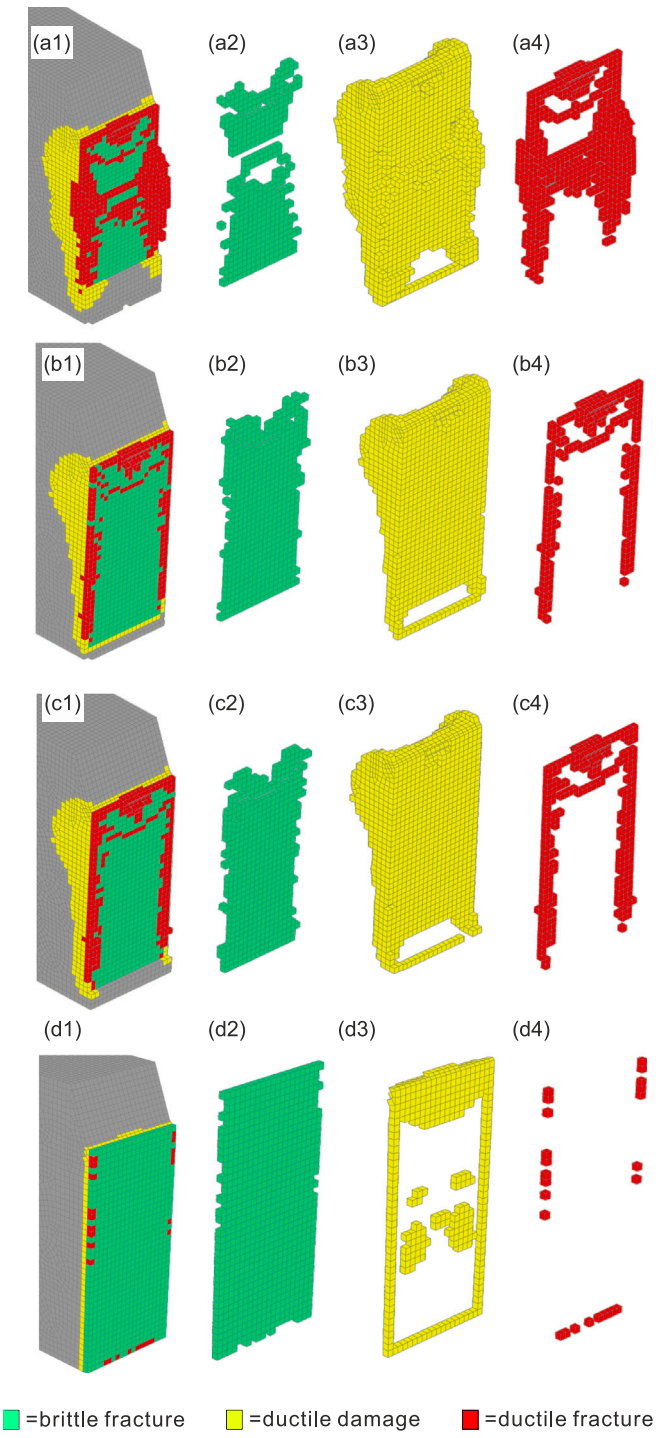


Fig. 15. Distribution of brittle fracture(a2–d2), damage (a3–d3) and ductile fracture (a4–d4) over the notched cross-section: (a1–a2) 25 °C, (b1–b2) −82 °C, (c1–c2) −92 °C, (d1–d2) −196 °C.

force–displacement curves in Fig. 10(e) and (h), where no zigzag behavior is detected at −92 °C, confirming the SEM findings. The numerically predicted ratio of brittle fracture to total fracture, shown in Fig. 16(a), increases from 52% at −51 °C to 66% at −92 °C, which agrees with the SEM observations showing an increasing fraction of brittle regions and fewer micro-voids. For the fracture surface at −145 °C, nearly pure cleavage is observed, with only a few small micro-voids, indicating a predominantly brittle fracture. Similarly, numerical analysis of the fractured elements, shown in Fig. 16(a), predicts approximately 90% brittle fracture, which is consistent with the experimental observations. The SEM images at different temperatures clearly reveal the ductile-to-brittle transition at the microscopic level, and the numerically predicted fracture behavior shows very good agreement with the experimental observations.

7. Conclusion

In this work, an advanced continuum damage and fracture framework is proposed to study the ductile-to-brittle transition behavior for the investigated high-strength low-alloy (HSLA) steel with a minimum yield strength of 1100 MPa. The behavior of plastic and damage is modeled using a modified Bai-Wierzbicki model that incorporates both damage and temperature effects. The ductile fracture behavior is captured by a modified Johnson–Cook-type fracture criterion that accounts for the influence of the third stress invariant through the Lode angle parameter. Brittle fracture is described by a modified principal stress–based Ritchie model, which includes the effects of temperature and damage. A single-step forward explicit Euler scheme is employed for numerical integration. In addition, the proposed material model has been implemented as a VUMAT subroutine in Abaqus.

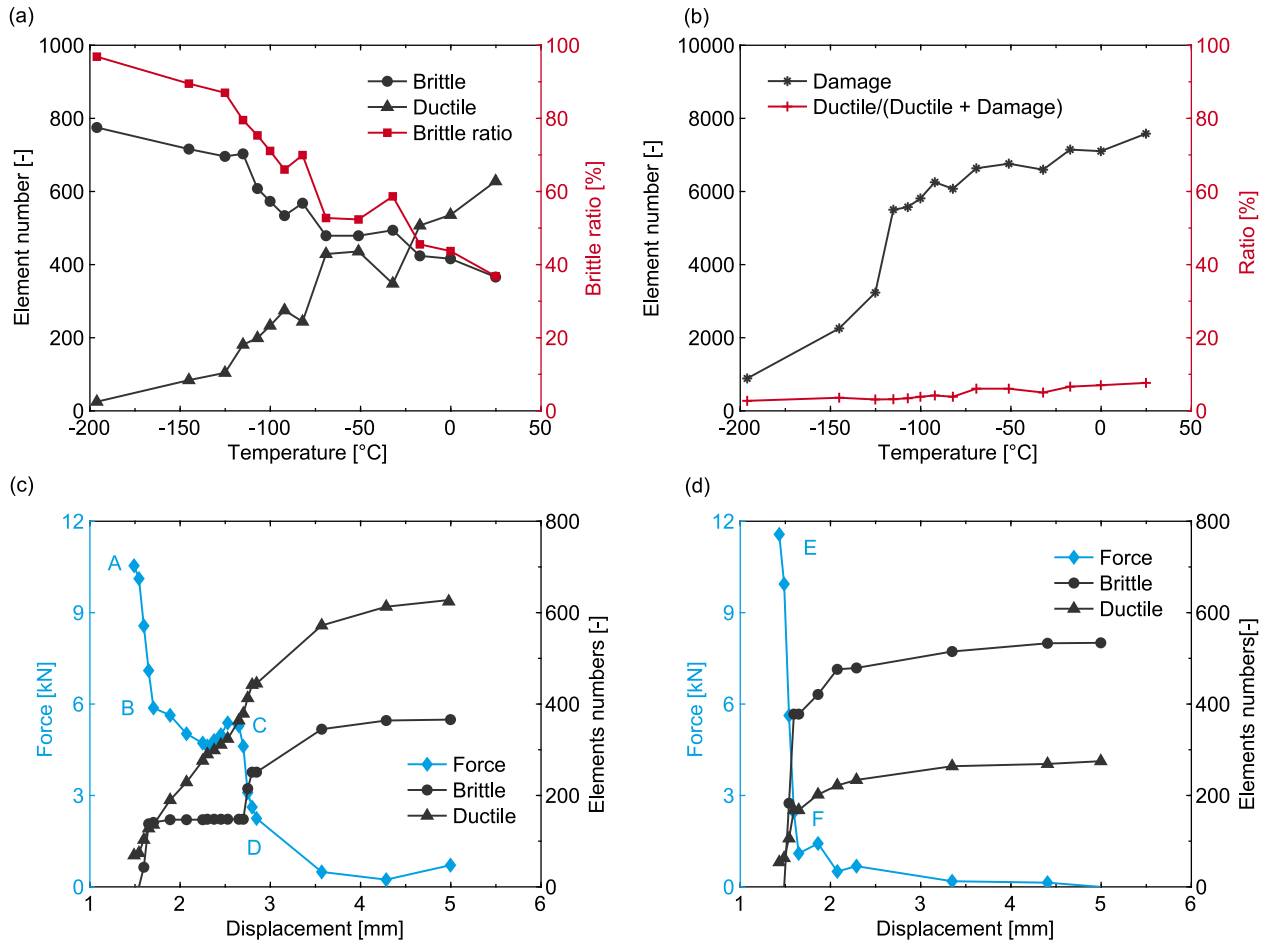


Fig. 16. Analysis of damage and fracture behavior based on the statistics of elements obtained from numerical simulations: (a) fracture behavior for all temperatures, (b) damage behavior for all temperatures, (c) fracture behavior at 25 °C, and (d) fracture behavior at −92 °C.

A systematic parameter identification strategy based on basic uniaxial experiments with different geometries was developed to generate a wide range of stress states and identify the corresponding elastic, plastic, damage, and fracture parameters. The proposed identification scheme effectively and accurately captures the required material parameters. The validation of the identified parameters through basic uniaxial loading experiments confirms the high accuracy and reliability of the material model with the calibrated parameters.

A series of sub-sized Charpy tests at 14 different temperatures, ranging from room temperature to −192 °C, were experimentally examined and numerically analyzed using the proposed continuum damage and fracture framework. The numerically predicted force–displacement response and impact energy show good agreement with the experimental results, confirming the significant influence of temperature on the ductile-to-brittle transition behavior. In addition, the numerical statistical analysis of damage, as well as brittle and ductile fracture elements, highlights the distinct mechanisms contributing to the material behavior at both the global force–displacement level and the microscopic scale, as confirmed by comparison with SEM observations of the fracture surfaces. Moreover, the numerical results further confirm that brittle fracture significantly contributes to the rapid force drop. The dominant fracture mechanism may shift between brittle and ductile behavior during different stages of crack initiation and propagation, as observed even at room temperature.

Although the numerical simulations in the present work agree well with the experimental results, mesh-size dependence remains due to the use of a local continuum damage formulation. For future work, nonlocal damage formulations (Wang et al., 2026; Papadioti et al., 2019; Davaze et al., 2021), phase-field approaches (Chu et al., 2019; Yin et al., 2025), or gradient damage models (Zhang et al., 2025) are suggested to predict damage and fracture behavior and to avoid mesh-size dependence and pathological strain localization after damage initiation. Moreover, DIC techniques can be used to identify an appropriate mesh size for more accurate results. For example, DIC-based parameter identification has been successfully applied in local damage formulations to predict a wide range of experiments under different complex loading conditions (Wei et al., 2025a). In addition, strain-rate effects on damage evolution and crack propagation are neglected in this paper, since the present work focuses on using a continuum damage model combined with ductile and brittle fracture criteria to predict crack initiation rather than accurately modeling crack propagation. The current framework is sufficient for engineering applications within acceptable error limits. Further improvements, including a more accurate energy-based characterization of the ductile-to-brittle transition, will be addressed in future work.

CRediT authorship contribution statement

Zhichao Wei: Writing – original draft, Visualization, Software, Methodology, Investigation, Formal analysis, Data curation, Conceptualization. **Guoxi Mao:** Writing – original draft, Software, Investigation, Formal analysis, Data curation. **Dongsong Li:** Writing – review & editing, Investigation, Data curation. **Berk Tekkaya:** Writing – review & editing. **Sophie Stebner:** Writing – review & editing. **Sebastian Münstermann:** Writing – review & editing, Resources, Project administration, Funding acquisition.

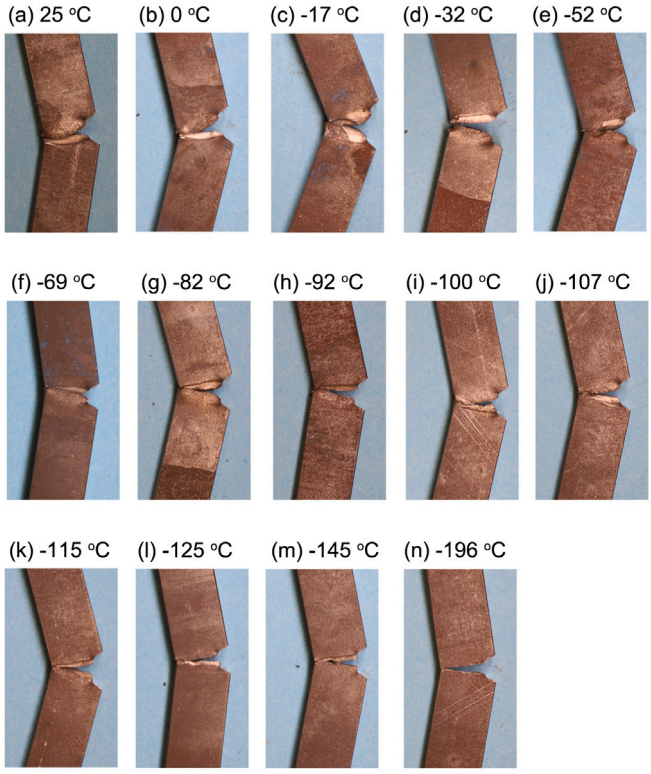


Fig. 17. Fracture photos of the sub-size Charpy experiments under different temperatures.

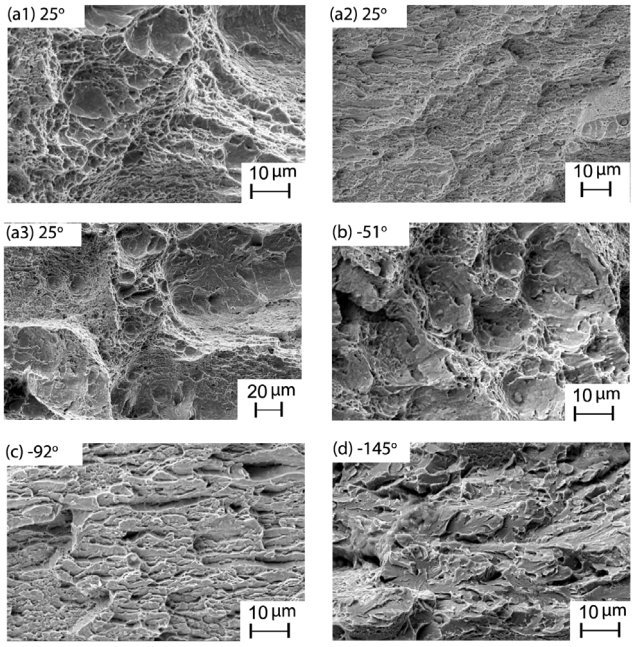


Fig. 18. Representative SEM image of the notched cross-section from the sub-sized Charpy specimen.

Declaration of competing interest

The authors declare that they have no known competing financial interests or personal relationships that could have appeared to influence the work reported in this paper.

Acknowledgments

The project has been funded by the AiF-Forschungsvereinigung (FV) – project number Nr. 21464 N, this financial support is gratefully acknowledged. We thank voestalpine AG and thyssenkrupp AG for providing the research material and IWT-Solutions AG for valuable discussions and advice. The authors gratefully acknowledge the computing resources provided by RWTH Aachen University, Germany, under projects rwth1791 and rwth1654.

Appendix A. Supplementary data

The user-defined VUMAT code has been uploaded as supplementary material and is available online through https://github.com/ibf-RWTH/MBW-Damage.

Data availability

Data will be made available on request.

References

Bai, Y., Wierzbicki, T., 2008. A new model of metal plasticity and fracture with pressure and lode dependence. Int. J. Plast. 24, 1071–1096.
Bai, Y., Wierzbicki, T., 2010. Application of extended mohr–Coulomb criterion to ductile fracture. Int. J. Fract. 161, 1–20.
Bao, Y., Wierzbicki, T., 2004. On fracture locus in the equivalent strain and stress triaxiality space. Int. J. Mech. Sci. 46, 81–98.
Beremin, F., Pineau, A., Mudry, F., Devaux, J., D'Escatha, Y., Ledermann, P., 1983. A local criterion for cleavage fracture of a nuclear pressure vessel steel. Metall. Trans. A 14, 2277–2287.
Brünig, M., 1999. Large strain elastic-plastic theory and nonlinear finite element analysis based on metric transformation tensors. Comput. Mech. 24, 187–196.
Brünig, M., 2003. An anisotropic ductile damage model based on irreversible thermodynamics. Int. J. Plast. 19, 1679–1713.
Chu, D., Li, X., Liu, Z., Cheng, J., Wang, T., Li, Z., Zhuang, Z., 2019. A unified phase field damage model for modeling the brittle-ductile dynamic failure mode transition in metals. Eng. Fract. Mech. 212, 197–209.
Davaze, V., Vallino, N., Langrand, B., Besson, J., Feld-Payet, S., 2021. A non-local damage approach compatible with dynamic explicit simulations and parallel computing. Int. J. Solids Struct. 228, 110999.
Gurson, A., 1977. Continuum theory of ductile rupture by void nucleation and growth: part I—yield criteria and flow rules for porous ductile media. J. Eng. Mater. Technol. 99, 2–15.
Habibi, N., Beier, T., Lian, J., Tekkaya, B., Koenemann, M., Muenstermann, S., 2024. Effects of damage evolution on edge crack sensitivity in dual–phase steels 95.. Steel Res. Int. 95, 2400178.
He, J., Lian, J., Golisch, G., Jie, X., Münstermann, S., 2017. A generalized orowan model for cleavage fracture. Eng. Fract. Mech. 186, 105–118.
Hütter, G., Linse, T., Roth, S., Mühlich, U., Kuna, M., 2014. A modeling approach for the complete ductile–brittle transition region: cohesive zone in combination with a non-local gurson-model. Int. J. Fract. 185, 129–153.
Johnson, G., Cook, W., 1985. Fracture characteristics of three metals subjected to various strains, strain rates, temperatures and pressures. Eng. Fract. Mech. 21, 31–48.
Khan, A., Liu, H., 2012. A new approach for ductile fracture prediction on al 2024-t351 alloy. Int. J. Plast. 35, 1–12.
Kotrechko, S., Strnadel, B., Dlouhý, I., 2007. Fracture toughness of cast ferritic steel applying local approach. Theor. Appl. Fract. Mech. 47, 171–181.
Krajcinovic, D., Fonseka, G., 1981. The continuous damage theory of brittle materials, part 1: general theory. J. Appl. Mech. 48, 809–815.
Leckie, F., Hayhurst, D., 1977. Constitutive equations for creep rupture. Acta Metall. 25, 1059–1070.
Lemaitre, J., Dufailly, J., 1987. Damage measurements, 28, 643–661. Eng. Fract. Mech. 28, 643–661.
Lian, J., Sharaf, M., Archie, F., Münstermann, S., 2013. A hybrid approach for modelling of plasticity and failure behaviour of advanced high-strength steel sheets. Int. J. Damage Mech. 22, 188–218.
Lian, J., Wu, J., Münstermann, S., 2015. Evaluation of the cold formability of high-strength low-alloy steel plates with the modified bai–wierzbicki damage model. Int. J. Damage Mech. 24, 383–417.
Lou, Y., Chen, L., Clausmeyer, T., Tekkaya, A., Yoon, J., 2017. Modeling of ductile fracture from shear to balanced biaxial tension for sheet metals. Int. J. Solids Struct. 112, 169–184.

Lou, Y., Huh, H., 2013. Extension of a shear-controlled ductile fracture model considering the stress triaxiality and the lode parameter. Int. J. Solids Struct. 50, 447–455.
Lou, Y., Wu, P., Zhang, C., Wang, J., Li, X., Chai, R., Yoon, J., 2022. A stress-based shear fracture criterion considering the effect of stress triaxiality and lode parameter. Int. J. Solids Struct. 256, 111993.
Lou, Y., Yoon, J., 2018. Anisotropic yield function based on stress invariants for BCC and FCC metals and its extension to ductile fracture criterion. Int. J. Plast. 101, 125–155.
Mohr, D., Marcadet, S., 2015. 2015. micromechanically-motivated phenomenological hosford–Coulomb model for predicting ductile fracture initiation at low stress triaxialities. Int. J. Solids Struct. 67-68, 40–55.
Nahshon, K., Hutchinson, J., 2008. Modification of the gurson model for shear failure. Eur. J. Mech. A Solids 27, 1–17.
Needleman, A., Tvergaard, V., 2000. Numerical modeling of the ductile-brittle transition. Int. J. Fract. 101, 73–97.
Oldfield, W., 1979. Fitting curves to toughness data. J. Test. Eval. 7, 326–333.
Pan, B., Zhu, L., Wei, Z., Tekkaya, B., Stebner, S., Münstermann, S., 2025. Analyses of stress-state-dependent ductile damage and fracture behavior of zirconium. Materials 19.
Papadioti, I., Aravas, N., Lian, J., Münstermann, S., 2019. A strain-gradient isotropic elastoplastic damage model with j3 dependence. Int. J. Solids Struct. 174–175, 98–127.
Pineau, A., 2008. Modeling ductile to brittle fracture transition in steels—micromechanical and physical challenges. Int. J. Fract. 150, 129–156.
Rice, J., Tracey, D., 1969. 1969. on the ductile enlargement of voids in triaxial stress fields. J. Mech. Phys. Solids 17, 201–217.
Ritchie, R., Knott, J., Rice, J., 1973. On the relationship between critical tensile stress and fracture toughness in mild steel. J. Mech. Phys. Solids 21, 395–410.
Shen, F., Sparrer, Y., Rao, J., Könemann, M., Münstermann, S., Lian, J., 2024. A forming limit framework accounting for various failure mechanisms: localization, ductile and cleavage fracture. Int. J. Plast. 103921.
Spitzig, W., Richmond, O., 1984. The effect of pressure on the flow stress of metals. Acta Metall. 32, 457–463.
Stoughton, T., Yoon, J., 2011. A new approach for failure criterion for sheet metals. Int. J. Plast. 27, 440–459.
Tanguy, B., Besson, J., Piques, R., Pineau, A., 2005. Ductile to brittle transition of an A508 steel characterized by charpy impact test. Eng. Fract. Mech. 72, 413–434.
Tlatlik, J., Hohe, J., Münstermann, S., 2023. Analysis and improvement of local cleavage fracture models at elevated loading rates. Theor. Appl. Fract. Mech. 125, 103857.
Türtük, İ., Deliktaş, B., 2016. Coupled porous plasticity – continuum damage mechanics approaches for modelling temperature driven ductile-to-brittle transition fracture in ferritic steels. Int. J. Plast. 77, 246–261.
Tvergaard, V., Needleman, A., 1984. Analysis of the cup-cone fracture in a round tensile bar. Acta Metall. 32 (1), 157–169.
Voyiadjis, G., Hoseini, S., Farrahi, G., 2013. A plasticity model for metals with dependency on all the stress invariants. J. Eng. Mater. Technol. 135, 011002.
Wallin, K., 2020. Sub-sized and miniature cvn specimen conversion methodology. Int. J. Press. Vessels Pip. 183, 104080.
Wang, S., Efsing, P., Faleskog, J., 2026. A non-local gtn model with two length scales calibrated for a low alloy steel. Mech. Mater. 214, 105579.
Wei, Z., Gerke, S., Brünig, M., 2023. Damage and fracture behavior under non-proportional biaxial reverse loading in ductile metals: Experiments and material modeling. Int. J. Plast. 171, 103774.
Wei, Z., Gerke, S., Brünig, M., 2024a. Ductile damage and fracture characterizations in bi-cyclic biaxial experiments. Int. J. Mech. Sci. 276, 109380.
Wei, Z., Gerke, S., Brünig, M., 2024c. Numerical analysis of non-proportional biaxial reverse experiments with a two-surface anisotropic cyclic plasticity-damage approach. Comput. Methods Appl. Mech. Eng. 419, 116630.
Wei, Z., Gerke, S., Brünig, M., 2025a. Novel uniaxial and biaxial reverse experiments for material parameter identification in an advanced anisotropic cyclic plastic-damage model. Mech. Mater. 205, 105294.
Wei, Z., Harting, M., Gerke, S., Brünig, M., 2025b. Ductile damage analysis under extreme low-cycle biaxial shear loadings: Experiments and simulations. Int. J. Solids Struct. 313, 113292.
Wei, Z., Koirala, S., Gerke, S., Brünig, M., 2026. Numerical analysis of anisotropic plasticity and damage based on the inelastic predictor-elastic corrector method. Int. J. Solids Struct. 326, 113770.
Wei, Z., Li, D., Mao, G., Münstermann, S., 2025c. Experimental analysis of the ductile-to-brittle transition in high-strength thin metal sheets: Charpy and novel impact tensile tests. Exp. Mech. 65, 1443–1460.
Wei, Z., Mao, G., Gerke, S., Münstermann, S., Brünig, M., 2025d. Experimental analysis and modeling of anisotropic ductile damage in non-proportional extreme low-cycle biaxial loading with shear-tension histories. Int. J. Plast. 194, 104474.
Wei, Z., Zistl, M., Gerke, S., Brünig, M., 2022. Analysis of ductile damage and fracture under reverse loading. Int. J. Mech. Sci. 228, 107476.
Wu, P., Lou, Y., 2025. Stress–based fracture model to describe ductile fracture behavior in various stress states. Fatigue. Fract. Eng. Mat. Struct. 48, 1200–1214.
Wu, P., Zhang, C., Lou, Y., 2023. Two-component DF2016 criterion to characterize the fracture behavior of magnesium rare-earth alloys. Theor. Appl. Fract. Mech. 127, 103677.
Wu, H., Zhuang, X., Zhao, Z., 2022. Extended GTN model for predicting ductile fracture under a broad range of stress states. Int. J. Solids Struct. 239–240, 111452.
Xue, L., 2008. Eng. Fract. Mech. 75, 3343–3366,
Yin, Y., Yu, H., Yan, H., Zhu, S., 2025. Diffusive-length-scale adjustable phase field fracture model for large/small structures. Int. J. Mech. Sci. 285, 109839.
Zeng, C., Fang, X., Habibi, N., Münstermann, S., Lian, J., 2024. A rate-dependent damage mechanics model for predicting plasticity and ductile fracture behavior of sheet metals at high strain rates. Eng. Fract. Mech. 306, 110217.
Zhang, Q., Ritzert, S., Zhang, J., Kehls, J., Reese, S., Brepols, T., 2025. A multi-field decomposed model order reduction approach for thermo-mechanically coupled gradient-extended damage simulations. Comput. Methods Appl. Mech. Eng. 434, 117535.
Zistl, M., Brünig, M., Gerke, S., 2024. Damage and fracture initiation under shear and compression stress states in the aluminum alloy EN aw6082-T6. Theor. Appl. Fract. Mech. 130, 104339.